

Spatial distribution of NH₂D in massive star-forming regions

Yuqiang Li^{1,2,*}, Junzhi Wang^{3,†}, Juan Li^{1,‡}, Shu Liu⁴, Kai Yang⁵, Siqu Zheng^{1,2}, Zhe Lu⁶

¹Shanghai Astronomical Observatory, Chinese Academy of Sciences, 80 Nandan Road, Shanghai 200030, China

²University of Chinese Academy of Sciences, 19A Yuquanlu, Beijing 100049, China

³Guangxi Key Laboratory for Relativistic Astrophysics, Department of Physics, Guangxi University, Nanning 530004, PR China

⁴CAS Key Laboratory of FAST, National Astronomical Observatories, Chinese Academy of Sciences, Beijing 100012, China

⁵School of Astronomy and Space Science, Nanjing University, 163 Xianlin Avenue, Nanjing 210023, China

⁶Department of Electrical and Electronic Engineering, Guilin University of Technology at Nanning, 530001, China.

Accepted XXX. Received YYY; in original form ZZZ

ABSTRACT

To understand the relation between NH₂D and its physical environment, we mapped ortho-NH₂D $1_{11}^s - 1_{01}^a$ at 85.9 GHz toward 24 Galactic late-stage massive star-forming regions with Institut de Radioastronomie Millimétrique (IRAM) 30-m telescope. Ortho-NH₂D $1_{11}^s - 1_{01}^a$ was detected in 18 of 24 sources. Comparing with the distribution of H¹³CN 1-0 as a dense gas tracer and radio recombination line H42 α , ortho-NH₂D $1_{11}^s - 1_{01}^a$ present complex and diverse spatial distribution in these targets. 11 of the 18 targets, present a different distribution between ortho-NH₂D $1_{11}^s - 1_{01}^a$ and H¹³CN 1-0, while no significant difference between these two lines can be found in other 7 sources, mainly due to limited spatial resolution and sensitivity. Moreover, with H42 α tracing massive young stellar objects, ortho-NH₂D $1_{11}^s - 1_{01}^a$ seems to show a relatively weak emission near the massive young stellar objects.

Key words: ISM: abundances—ISM: molecules—Stars: formation—Stars: massive

1 INTRODUCTION

Deuterium chemistry is an active process in molecular clouds (Caselli et al. 2008). The deuterated molecules, such as DCN, DCO⁺, N₂D⁺ and NH₂D, can be formed at different evolution stages of star-forming (Caselli et al. 2008). Due to the relatively low zero-point energy, these deuterated molecules are generated more easily in molecular clouds (Herbst 1982). Therefore, the deuterium fractionation (D_{frac}), as the ratio between deuterated and normal molecule, is often higher than the D/H ratio of $\approx 1.5 \times 10^{-5}$ (Linsky et al. 1995; Oliveira et al. 2003).

Deuterated ammonia (NH₂D, NHD₂ and ND₃) can form in different ways: 1) The deuterated ions (D) take the place of hydrogen (H) in the ammonia in the gas phase (Rodgers & Charnley 2001; Caselli et al. 2008; Caselli & Ceccarelli 2012; Ceccarelli et al. 2014). 2) The reaction between deuterated ions and NH₃. For cold regions (T<30K), H₂D⁺ react with NH₃, while in warm regions (T=30-80 K), the CH₂D⁺ and C₂HD⁺ react with NH₃ to generate deuterated ammonia (Roberts & Millar 2000a,b; Caselli & Ceccarelli 2012; Ceccarelli et al. 2014). 3) The reactions with H, D and N atoms are also an effective approach (Brown & Millar 1989; Fedoseev, Ioppolo, & Linnartz 2015). 4) The chemical reaction of deuteration could happen on the surface of dust grains if the reactions of the gas phase are unavailable (Turner 1990; Cazaux et al. 2003; Caselli et al. 2008).

5) In addition, shocks may be associated with the enhancement of deuterated species (Lis et al. 2002).

As a single deuterated form molecule, NH₂D was detected extensively in the molecular cloud. $D_{\text{frac}}(\text{NH}_3)$ was observed to be $\sim 1 - 0.1$ in the cold environment (e.g. Hatchell 2003; Crapsi et al. 2007; Harju et al. 2017) and $\sim 0.1 - 0.001$ in the warm environment (e.g. Busquet et al. 2010; Pillai et al. 2011; Gong et al. 2015). Besides, with the model calculations, deuterium fractionation is sensitive to its environment changes, such as temperature and density (Roberts & Millar 2000a,b).

According to the high-resolution radio observation in late-stage massive star-forming regions, a series of the researches have reported the relation between NH₂D and its physical environment. With the IRAM Plateau de Bure Interferometer (PdBI), Busquet et al. (2010) observed the ortho-NH₂D $1_{11}^s - 1_{01}^a$ at 85.9263 GHz in the ultracompact HII region (UCHII region) IRAS 20293+3952, through which they reported that the $D_{\text{frac}}(\text{NH}_3)$ in young stellar objects (YSOs) was lower than in pre-protostellar cores, and the $D_{\text{frac}}(\text{NH}_3)$ could be related to the evolutionary stage in the pre-protostellar phase. With AtacamaLarge Millimeter/Submillimeter Array (ALMA) observation of Orion KL Hot Core and Compact Ridge for NH₂D at 239.848 GHz, Neill et al. (2013) found that the deuterium fractionation in Orion KL Hot Core was lower than that in Compact Ridge, suggesting that the hot core originated in a slightly warmer environment result in low deuterium fractionation. Mills et al. (2018) reported that the $D_{\text{frac}}(\text{NH}_3)$ of Sgr B2(N2) is ≈ 10 times higher than that of Sgr B2(N1) with VLA observations of the NH₂D $4_{14}^s - 4_{04}^a$ transitions at 25.0 GHz and ATCA observations of the NH₂D $2_{12}^a - 2_{02}^s$ transitions at 49.9 GHz and the NH₂D $3_{13}^s - 3_{03}^a$ transitions at 43.0 GHz, so

* E-mail: liyuqiang@shao.ac.cn

† E-mail: junzhiwang@gxu.edu.cn

‡ E-mail: lijuan@shao.ac.cn

that they attributed the abundance variations to the shock and fast warmup in Sgr B2(N2). However, the researches mentioned above are only based on one or two sources (Busquet et al. 2010; Neill et al. 2013; Mills et al. 2018). Consequently, a relatively large sample of massive star-forming regions is needed to understand the relation between NH₂D and its physical environment.

NH₂D $1_{11}^a - 1_{01}^s$ at 110.1535 GHz with single point observations using Institut de Radioastronomie Millimétrique (IRAM) 30-m telescope toward 50 late-stage massive star-forming regions was reported with 72% detection rate (Li et al. 2022). With stronger emission (e.g. Shah & Wootten 2001; Wiene et al. 2021), ortho-NH₂D $1_{11}^s - 1_{01}^a$ at 85.9263 GHz is more suitable than para-NH₂D $1_{11}^a - 1_{01}^s$ at 110.1535 GHz to derive NH₂D spatial distribution. Therefore, we mapped the ortho-NH₂D $1_{11}^s - 1_{01}^a$ at 85.9263 GHz in late-stage high mass star-forming regions with IRAM 30-m to obtain spatial distribution information of NH₂D.

With IRAM 30-m telescope observation, this work presents the results of ortho-NH₂D $1_{11}^s - 1_{01}^a$ at 85.9263 GHz mapping toward a relatively large sample of 18 Galactic late-stage massive star-forming regions with known 6.7 GHz CH₃OH masers. The observations are described in Section 2, the main results are reported in Section 3, a discussion is presented in Section 4, and a brief summary is given in Section 5.

2 OBSERVATIONS

The 24 targets, selected from Reid et al. (2014), are late-stage massive star-forming regions with 6.7 GHz CH₃OH masers with HC₃N 12-11 higher than 1 K (T_{mb}) which is based on IRAM 30-m observations. The observations were performed with the Institut de Radioastronomie Millimétrique (IRAM) 30-m telescope at Pico Veleta, Spain during 2019 July, 2019 October, 2019 November, 2020 December and 2021 January. The on-the-fly (OTF) mode was used in our observations with the frequency coverage about 8 GHz bandwidth. The system temperatures were 80-150 K during our observation. We used the E090 receiver to cover 84 GHz to 92 GHz and the Fourier Transform Spectrometers (FTS) backend with a 195 kHz channel spacing, which corresponds to 0.68 km s⁻¹ at 86 GHz. The map centers and map area are listed in table 1.

The antenna temperature (T_A^*) is converted to the main beam brightness temperature (T_{mb}), using $T_{\text{mb}} = T_A^* \cdot F_{\text{eff}}/B_{\text{eff}}$, the forward efficiency F_{eff} is 0.95 and the beam efficiency B_{eff} is 0.81. The used lines consist of ortho-NH₂D $1_{11}^s - 1_{01}^a$ at 85.9263 GHz, H¹³CN 1-0 at 86.3387 GHz and H42 α at 85.6884 GHz. Data reduction was conducted with GILDAS software¹. The angular resolution of the IRAM 30-m telescope is about 29.3 arcsec at 84 GHz and about 26.7 arcsec at 92 GHz, while all sources were re-gridded to steps of 9 arcsecs, about 1/3 beam size. First-order baseline was used for all spectra. The typical rms are around 50 mK at 0.7 km s⁻¹ velocity resolution. In the following analysis, we assume that the beam-filling factor is unity.

3 RESULTS

The ortho-NH₂D $1_{11}^s - 1_{01}^a$ at 85.9263 GHz was detected among 18 targets of our sample, while it was not detected in the rest six targets: G009.62+00.19, G011.49-014.8, G012.80-00.20, G043.16+00.01,

G133.94+01.06 and G192.60-00.04. For ortho-NH₂D detected targets, the H¹³CN 1-0 was also detected, while H42 α was detected only in nine targets.

11 of 18 sources, present a different distribution between ortho-NH₂D $1_{11}^s - 1_{01}^a$ and H¹³CN 1-0 with asymmetrically and resolvable distributed spatial structure. Due to limited sensitivity, the structure of ortho-NH₂D $1_{11}^s - 1_{01}^a$ at 85.9263 GHz was unresolved in G005.88-00.39 and G188.94+00.88 (see Figure 1 and Figure 18). For 4 sources, G011.91-00.61, G023.44-00.18, G034.39+00.22 and G049.48-00.38 (see Figure 2, Figure 4, Figure 6 and Figure 11), no significant difference between these two lines can be found. It is mainly due to the limited spatial resolution. Only one target, G081.75+00.59 (see Figure 13), presents a relatively similar distribution between ortho-NH₂D $1_{11}^s - 1_{01}^a$ at 85.9263 GHz and H¹³CN 1-0 and resolvable distributed spatial structure.

The detailed results of the three lines are given in Section 3.1-3.4, the ortho-NH₂D $1_{11}^s - 1_{01}^a$, H¹³CN 1-0 and H42 α distribution details of each source are described in Section 3.5.

3.1 NH₂D spatial distribution

The velocity integrated intensity of ortho-NH₂D $1_{11}^s - 1_{01}^a$ at 85.9263 GHz, observed with the IRAM-30m, are presented in Figure 1 - 18 as red contour. The spectra of ortho-NH₂D $1_{11}^s - 1_{01}^a$ at 85.9263 GHz are also presented in Figure 1 - 18. For overlaying with H¹³CN 1-0 spectra, there are some of the sources in which several offsets are shown in Figure 1 - 18. These several offsets are used to confirm the signal of ortho-NH₂D $1_{11}^s - 1_{01}^a$ emission if this target has spatial structures, such as G081.75+00.59 (see Figure 13).

Ortho-NH₂D $1_{11}^s - 1_{01}^a$ has six hyperfine structures, with relative intensities listed in Table 2 (Tin e et al. 2000). However, the transitions of F=2-1, F=2-2, F=1-1 and F=1-2 for ortho-NH₂D $1_{11}^s - 1_{01}^a$ are blended due to line broadening. For example, as shown in Figure 19, only three components can be found in G081.75+00.59 for NH₂D spectra. Thus, the fluxes of ortho-NH₂D $1_{11}^s - 1_{01}^a$ were derived with the velocity integrated intensity of the emitting channels of its six hyperfine structures instead of Gaussian fitting. In the following analysis, we assume all NH₂D spectra are optically thin.

Four sources, G011.91-00.61, G023.44-00.18, G034.39+00.22 and G049.48-00.38, are not detected asymmetrically distributed spatial structure of ortho-NH₂D (see Figure 2, Figure 4, Figure 6 and Figure 11, respectively). Ortho-NH₂D emissions were marginally detected and unresolved in two targets: G005.88-00.39 and G188.94+00.88 (see Figure 1 and Figure 18). In addition, although G015.03-00.67 and G037.43+01.51 (see Figure 3 and Figure 9) can be distinguished the spatial structure, the ortho-NH₂D emissions are weak. Other targets can be distinguished the spatial structure and detected relatively strong ortho-NH₂D emission.

The strongest velocity integrated intensity and distribution shape of ortho-NH₂D for each source are listed in Table 4. The strongest ortho-NH₂D emission is 6.95±0.14 K km/s in G081.75+00.59 and the weakest ortho-NH₂D emission is 0.60±0.16 and 0.60±0.11 K km/s in G005.88-00.39 and G037.43+01.51, respectively. The median of ortho-NH₂D emission is 2.27 K km/s. For the sources whose ortho-NH₂D emission is lower than 1 K km/s, are considered as sources with weak NH₂D emission. Conversely, we define strong NH₂D emissions to be cases surpassing the 1 K km/s threshold. Accordingly, there are 4 sources characterized by weak NH₂D emissions and 14 sources are classified into strong NH₂D emissions.

With strong NH₂D emission detected, 14 sources show complex and diverse distribution, which is different from other molecule tran-

¹ <http://www.iram.fr/IRAMFR/GILDAS>

sitions, such as the dense gas tracer H¹³CN 1-0 (details described in the following).

3.2 The ortho-to-para ratio of NH₂D

We presented single point observational results of para-NH₂D $1_{11}^a - 1_{01}^s$ at 110.1535 GHz with IRAM-30m toward 50 late-stage massive star-forming regions (Li et al. 2022), which included all the targets of this work. The NH₂D spectra, both of the ortho-NH₂D $1_{11}^s - 1_{01}^a$ at 85.9263 GHz with OTF mode and para-NH₂D $1_{11}^a - 1_{01}^s$ at 110.1535 GHz with position-switching mode, are also shown in figure 1 - 18. All coordinates of para-NH₂D $1_{11}^a - 1_{01}^s$ at 110.1535 GHz are consistent with offset (0'',0'') ortho-NH₂D $1_{11}^s - 1_{01}^a$ at 85.9263 GHz, except G011.91-00.61, G015.03-00.67 and G034.39+00.22. Para-NH₂D $1_{11}^a - 1_{01}^s$ at 110.1535 GHz transition have offset about (-27'',-27''), (45'',36'') and (0'',-45''), corresponding to ortho-NH₂D $1_{11}^s - 1_{01}^a$ at 85.9263 GHz in G011.91-00.61 (see Figure 2), G015.03-00.67 (see Figure 3) and G034.39+00.22 (see Figure 6), respectively.

For two hydrogen atoms in NH₂D, different nuclear spin angular momentum can produce different states: ortho and para state. The ortho state has the largest nuclear spin statistical weight, and the para state has the largest nuclear spin statistical weight (Harju et al. 2017). Since normal radiative and collisional transitions can not change the spin of H nuclei, the transitions between ortho- and para-NH₂D are forbidden (Ho & Townes 1983). Therefore, obtaining ortho- and para-NH₂D could reflect an accurate abundance of NH₂D.

The corresponding nuclear statistical weights are 27 and 9 for ortho-NH₂D $1_{11}^s - 1_{01}^a$ at 85.9263 GHz and para-NH₂D $1_{11}^a - 1_{01}^s$ at 110.1535 GHz, respectively (CDMS², Müller et al. (2001, 2005)). Therefore, the ratio of N(ortho-NH₂D)/N(para-NH₂D) is 3 in LTE and this ratio could indicate the discrepancy between total column density and ortho-NH₂D or para-NH₂D. The Einstein emission coefficient is $7.8214 \times 10^{-6} \text{ s}^{-1}$ and $1.6503 \times 10^{-5} \text{ s}^{-1}$ for ortho-NH₂D $1_{11}^s - 1_{01}^a$ at 85.9263 GHz and para-NH₂D $1_{11}^a - 1_{01}^s$ at 110.1535 GHz, respectively (CDMS, Müller et al. (2001, 2005)). In addition, the line ratios of velocity integrated intensities between ortho-NH₂D $1_{11}^s - 1_{01}^a$ at 85.9263 GHz and para-NH₂D $1_{11}^a - 1_{01}^s$ at 110.1535 GHz is also related to the excitation temperature. Considering Einstein emission coefficient, the line ratios of velocity integrated intensities between ortho-NH₂D $1_{11}^s - 1_{01}^a$ at 85.9263 GHz and para-NH₂D $1_{11}^a - 1_{01}^s$ at 110.1535 GHz is about 2.5 at 10 K and 2.4 at 20 K at LTE.

The line ratios of velocity integrated intensities between ortho-NH₂D $1_{11}^s - 1_{01}^a$ at 85.9263 GHz and para-NH₂D $1_{11}^a - 1_{01}^s$ at 110.1535 GHz are listed in Table 3. The ortho-NH₂D $1_{11}^s - 1_{01}^a$ at 85.9263 GHz spectra from the mapping results at the same position as that of para-NH₂D $1_{11}^a - 1_{01}^s$ at 110.1535 GHz are used for this comparison. Upper limits are provided in six sources due to non-detection of ortho-NH₂D $1_{11}^s - 1_{01}^a$ or para-NH₂D $1_{11}^a - 1_{01}^s$ lines, in where coordinate is para-NH₂D $1_{11}^a - 1_{01}^s$. The highest ratio is 4.73 ± 1.99 in G035.20-01.73 and the lowest ratio is 0.89 ± 0.44 in G005.88-00.39, both of them are with strong H42 α emissions. In other sources, this ratio ranges from 1.26 ± 0.07 to 2.95 ± 0.12 . Besides, the median of this ratio is 1.84.

² <https://cdms.astro.uni-koeln.de/classic/predictions/catalog/>

3.3 H¹³CN 1-0 maps result

HCN lines can be used to trace dense gas ($\gtrsim 10^4 \text{ cm}^{-3}$) because of high dipole moment and large Einstein A-coefficient (Evans et al. 2006). With the similar dipole moment and Einstein A-coefficient, lines of H¹³CN, as an isotope molecule of HCN, can be used as a dense gas tracer. So, H¹³CN lines can be more accurate to trace dense molecular gas, since they are mainly optically thin. Therefore, H¹³CN 1-0 is used as a dense gas tracer (Gao & Solomon 2004; Wu et al. 2010; Vasyunina et al. 2011).

In this work, the H¹³CN 1-0 emission was detected in all targets. H¹³CN 1-0 has three hyperfine structures. Similar to ortho-NH₂D $1_{11}^s - 1_{01}^a$, the velocity integrated intensity of H¹³CN 1-0 was derived from its three hyperfine structures with CLASS/GILDAS package. The mapping results and spectra of H¹³CN 1-0 are shown in Figure 1 - 18 (black contour and gray scale).

Table 4 lists whether ortho-NH₂D and H¹³CN 1-0 show similar distribution or not in each source. Ortho-NH₂D and H¹³CN 1-0 are unresolved in two sources (G005.88-00.39 and G188.94+00.88, see Figure 1 and Figure 18), with weak ortho-NH₂D emissions in these two sources. Weak NH₂D emissions in G015.03-00.67 and G037.43+01.51 (see Figure 3 and Figure 9) were detected different distributions to that of H¹³CN 1-0. Among other sources with relatively strong ortho-NH₂D emission detected, five sources show similar distributions and nine show different distributions between NH₂D and H¹³CN 1-0 maps. G035.20-01.73, G075.76+00.33, G081.87+00.78 and G109.87+02.11 show that the distribution of strong NH₂D is dislocation with H¹³CN (see Figure 8, Figure 12, Figure 14 and Figure 15, respectively). In addition, in the targets of G031.28+00.06, G035.19-00.74, G075.76+00.33, G111.54+00.77 and G121.29+00.65, some regions present a strong NH₂D emission, while just weak H¹³CN 1-0 emission is detected in these regions (see Figure 5, Figure 7, Figure 12, Figure 16 and Figure 17, respectively).

In G011.91-00.61, G023.44-00.18, G034.39+00.22, G049.48-00.38 and G081.75+00.59, ortho-NH₂D present a similar distribution with H¹³CN 1-0 (see Figure 2, Figure 4, Figure 6, Figure 11 and Figure 13, respectively). The strong ortho-NH₂D emission was also detected in these five sources. The strongest NH₂D spectra was detected in G081.75+00.59 with $\int T_{\text{mb}}(\text{NH}_2\text{D})dv = 6.95 \pm 0.14 \text{ K km s}^{-1}$. However, the asymmetrically structure of ortho-NH₂D $1_{11}^s - 1_{01}^a$ at 85.9263 GHz was not detected in G011.91-00.61, G023.44-00.18, G034.39+00.22 and G049.48-00.38. The reason is mainly due to the limited spatial resolution. Only G081.75+00.59 present asymmetrically structure of ortho-NH₂D $1_{11}^s - 1_{01}^a$ at 85.9263 GHz.

3.4 H42 α maps result

The young massive stars, with spectral types of B or O, can produce ultra-violet photons, which can ionize the surrounding interstellar medium and create HII regions. Consequently, the abundantly ionized hydrogens exist in HII regions and can recombine with electrons to produce the radio recombination lines (RRLs). Therefore, the RRLs can be used to trace young massive star-forming and HII regions.

RRL H42 α was detected in nine sources (see also in figure 1 - 18, the black contour and gray scale). Without turbulence, the full width at half maxima (FWHM) of RRLs is 19.1 km s^{-1} at 8000 K (Peters, Longmore, & Dullemond 2012). Therefore, in the case of a faint RRLs signal observed in G031.28+00.06, the spectral resolution was smoothed to 1.4 km s^{-1} to confirm whether it is H42 α emission or not in the present work. Among these nine targets, a completely different spatial distribution between ortho-NH₂D and H42 α is presented in

five targets, while the spatial distribution of ortho-NH₂D and H42 α have overlapping regions in the rest four targets.

A strong H42 α emission presents in G005.88-00.39 (see Figure 1), while the ortho-NH₂D were marginally detected and almost unresolved in the same position. There are two NH₂D emission features and a relatively weak H42 α structure with associated NH₂D emission in G011.91-00.61 (see Figure 2). G049.48-00.36 and G049.48-00.38 are two adjacent sources (see Figure 10 and Figure 11). Both of them, the ortho-NH₂D and H42 α present different spatial distributions. However, the ortho-NH₂D emission peaks at the H42 α emission peak in G049.48-00.36. Besides, in G049.48-00.36, the ortho-NH₂D is weaker than that in G049.48-00.38.

In G015.03-00.67 (see Figure 3), a widely distributed and strong H42 α emission was detected, while the ortho-NH₂D is scattered in other positions. In G031.28+00.06 (see Figure 5), the ortho-NH₂D is isolated by H42 α and the emission of ortho-NH₂D is very weak. The H42 α are also observed in G035.20-01.73, G075.76+00.33 and G111.54+00.77 (see Figure 8, Figure 12 and Figure 16, respectively). The ortho-NH₂D and H42 α present a completely different spatial distribution in G035.20-01.73, G075.76+00.33 and G111.54+00.77, but the NH₂D emission is far away from the H42 α emission.

3.5 Individual target detail

In our observation, most sources show different spatial distributions between ortho-NH₂D and H¹³CN 1-0 emission, or between ortho-NH₂D and H42 α emission, while a few sources show similar spatial distributions. For example, the ortho-NH₂D and H¹³CN 1-0 emission present similar spatial distribution in G011.91-00.61. The details each source are described in following.

3.5.1 G005.88-00.39

G005.88-00.39 is a bright expanding shell-like UCHII region (Acord, Churchwell, & Wood 1998). According to near-infrared NACO-VLT observations, Feldt et al. (2003) suggested G005.88-00.39 contains a massive young O5 V star. Furthermore, this target is one of the most powerful outflows in Galaxy (Harvey & Forveille 1988; Zapata et al. 2020). In the present work, strong ($\int T_{\text{mb}}d\nu \geq 40 \text{ K km s}^{-1}$) H¹³CN 1-0 and H42 α emission were detected in G005.88-00.39, and their velocity integrated intensity maps(see figure 1). However, ortho-NH₂D at 85.9 GHz was only observed at the source center with a weak emission, which is the weakest among our samples. Therefore, the ortho-NH₂D may be marginally detected in this source and it was plotted from 2σ . Moreover, the ortho-NH₂D velocity integrated intensity mapping presents less than a beam, so the spatial structure might not be distinguished in G005.88-00.39. Due to the weak ortho-NH₂D emission and indistinguishable spatial structure, we can not confirm whether the distribution of ortho-NH₂D is similar to other molecules or not.

3.5.2 G011.91-00.61

With the H76 α detected, Wood & Churchwell (1989) indicated that an UCHII region exists in G11.94-00.62 (RA.(J2000)=18:14:01.006, DEC.(J2000)=-18:53:24.966), and Ilee et al. (2018) suggested that there was a proto-O star forming in this region. The distribution of ortho-NH₂D, H¹³CN 1-0 and H42 α (see figure 2) were obtained in G011.91-00.61. The ortho-NH₂D and H¹³CN 1-0 show two structures and similar distributions. However, only the structure in the northeast (G11.94-00.62) has been detected to have H42 α emission.

Although the intensity of H¹³CN 1-0 is similar in these two structures, the ortho-NH₂D appears weaker in the northeast structure where H42 α is detected.

3.5.3 G015.03-00.67

G015.03-00.67 (M 17) is a molecular cloud complex (Lada 1976) and it is the closest (1.98 kpc, Xu et al. (2011)) giant HII region to us (Lim, De Buizer, & Radomski 2020). Hundreds of candidate massive YSOs with spectral types have been found earlier than B9 in G015.03-00.67(Lada, Bally, & Stark 1991; Povich et al. 2009). We obtained a $4' \times 4'$ size map of ortho-NH₂D, H¹³CN 1-0 and H42 α toward IRAM 30m observation in G015.03-00.67 (see figure 3). The ortho-NH₂D was detected relatively weak emission in G015.03-00.67 ($\int T_{\text{mb}}(\text{NH}_2\text{D})d\nu=1.1 \text{ K km s}^{-1}$ in the strongest pixel). The ortho-NH₂D emission presents a fragmented distribution. A widely distributed H42 α distribution was detected in G015.03-00.67, indicating it is a giant HII region. The ortho-NH₂D fragments avoid obviously the widely distributed H42 α distribution. The widely distributed H¹³CN 1-0 emission was also detected in this target. One of the ortho-NH₂D fragments appears in the strongest H¹³CN 1-0 structure, others appear with relatively weak H¹³CN 1-0 emission. The strong H42 α emission is at the northeast of G015.03-00.67 where H¹³CN 1-0 is marginally or even not detected.

3.5.4 G023.44-00.18

The strong 6.7 GHz CH₃OH maser has been detected in the massive star-forming region G023.44-00.18 (Walsh et al. 1998). With Submillimeter Array (SMA) observation, Ren et al. (2011) reported that G023.44-00.18 presented two dust cores that were north and south arranged, the south one has active bipolar outflow. In addition, they suggested that these two dust cores were in the pre-UCHII evolutionary stage. By observing the ortho-NH₂D $1_{11}^s - 1_{01}^a$ at 85.9263 GHz toward PdBI, Zhang et al. (2020) found several NH₂D cores in G023.44-00.18 with $D_{\text{frac}} \sim 0.1$. But these cores are offset by two dust cores which are reported in Ren et al. (2011). However, because of the spatial resolution limitation, both ortho-NH₂D and H¹³CN 1-0 emission can not be distinguished by two cores in our observation, and H42 α was not detected (see Figure 4). Nevertheless, in the northwest of G023.44-00.18, the obvious NH₂D signal was detected with weak H¹³CN 1-0 emission.

3.5.5 G031.28+00.06

G031.28+00.06 is located in W43, which is a molecular cloud complex (Nguyen Luong et al. 2011). As is shown in figure 5, ortho-NH₂D, H¹³CN 1-0 and H42 α were detected in G031.28+00.06. The ortho-NH₂D emission presents two structures in this source, while H¹³CN 1-0 and H42 α (see figure 5) present one structure. Compared with other targets, the ortho-NH₂D and H42 α emission in G031.28+00.06 are relatively weak. Furthermore, two NH₂D structures seem to be isolated by the H42 α structure. Besides, the ortho-NH₂D and H¹³CN present a different distribution in this source.

3.5.6 G034.39+00.22

G034.39+00.22 is an UCHII region with 1000 M_⊙ mass (Miralles, Rodriguez, & Scalise 1994). With IRAM 30m observation, Rathborne, Jackson, & Simon (2006) reported 1.2 mm continuum maps in

G034.39+00.22 which present north to south distribution. They indicated that nine millimeter-dense clumps existed in G034.39+00.22. In the present work, we focus on the brightest region in G034.39+00.22. The distribution of strong ortho-NH₂D and H¹³CN 1-0 emission were detected in G034.39+00.22. These two lines present a north to south distribution (see figure 6). The distribution of ortho-NH₂D is similar to H¹³CN 1-0 in G034.39+00.22. Both ortho-NH₂D and H¹³CN appear two structures and show two peaks in this target. Besides, H42 α was not detected in G034.39+00.22.

3.5.7 G035.19-00.74

Dent, Little, & White (1984) reported that G035.19-00.74 was an UCHII region and contained a young B0 star. With James Clerk Maxwell Telescope (JCMT), Berkeley-Illinois-Maryland Association (BIMA) and VLA observation, Gibb et al. (2003) found CO outflow with $\sim 45^\circ$ along the northeast-southwest direction in G035.19-00.74. In our work, the distribution of strong ortho-NH₂D and H¹³CN 1-0 emission were detected in G035.19-00.74 while H42 α was not detected (see figure 7). The distribution of ortho-NH₂D is obviously different from H¹³CN 1-0. The H¹³CN 1-0 distribution seems like a core. However, the distribution of ortho-NH₂D is oriented northwest to the southeast which is perpendicular to the CO outflow reported in Gibb et al. (2003).

3.5.8 G035.20-01.73

G035.20-01.73 (W 48) contains an UCHII region (Wood & Churchwell 1989). The east to west evolutionary gradient was found in the HII region (Rygl et al. 2014). We obtained the H¹³CN 1-0, distributed from east to west with two strong peaks and a weak peak (see figure 8). Pillai et al. (2011) present the distribution of ortho-NH₂D at 85.9 GHz oriented west to east in G035.20-01.73 toward PdBI observations. Combined with the 3.5 mm dust emission map, they found the dust emission peak is not the brightest NH₂D peak in this target. H42 α is observed in G035.20-01.73, which is near from the center peak of H¹³CN 1-0 distribution (see figure 8). The ortho-NH₂D was also observed with strong emission (see figure 8). The ortho-NH₂D, away from the H42 α , is located in the west of G035.20-01.73 and shows a similar distribution to the result in Pillai et al. (2011). Besides, the NH₂D peak offsets H¹³CN 1-0 peak, while the NH₂D distribution is similar to the 3.5 mm dust emission in Pillai et al. (2011).

3.5.9 G037.43+01.51

With MPIFR 37-element bolometer array observation, Beuther et al. (2002) detected an extended 1.2 mm continuum core. Several deuterated molecules, HDCO and D₂CO (Zahorecz et al. 2021) and DC₃N (Rivilla et al. 2020) were detected in G037.43+01.51. In G037.43+01.51, the relatively weak ortho-NH₂D and H¹³CN 1-0 emission were detected, while H42 α was not detected (see figure 9). The H¹³CN 1-0 emission is similar to the 1.2 mm continuum map reported in Beuther et al. (2002). However, the spatial distribution of weak ortho-NH₂D emission appears to deviate from that of H¹³CN 1-0.

3.5.10 G049.48-00.36

G049.48-00.36 (W 51 IRS2) is one of the massive protocluster candidates in giant molecular cloud W51 (Ginsburg et al. 2012). W 51 is a

complex structure molecular cloud with several velocity components (Scoville & Solomon 1973). In the present work, the ortho-NH₂D and H¹³CN 1-0, H42 α (see figure 10) maps were obtained in G049.48-00.36. At the map center, the structures of the ortho-NH₂D, H¹³CN 1-0 and H42 α distribution are close. Although part of ortho-NH₂D emission is detected near one of the H42 α structures, most ortho-NH₂D emission distributions deviate from the H42 α emission. With strong emission, the ortho-NH₂D, H¹³CN 1-0 and H42 α were also detected in the southeast where G049.48-00.38 is located.

3.5.11 G049.48-00.38

G049.48-00.38 (W 51 M) is adjacent to G049.48-00.36 and it is also one of the massive protocluster candidates in W 51 (Ginsburg et al. 2012). As figure 11 shows, strong ortho-NH₂D and H¹³CN 1-0, H42 α were observed in this work (see figure 10). The ortho-NH₂D distribution is similar to H¹³CN 1-0, while the ortho-NH₂D and H¹³CN 1-0 emission offset H42 α peak. With the PdBI observations, Vastel et al. (2017) reported that ortho-NH₂D was detected in two marginally resolved sources, while we have detected only one here due to the spatial resolution limitation.

3.5.12 G075.76+00.33

With BIMA interferometer observation, Riffel & Lüdke (2010) mapped HCN 1-0 in G075.76+00.33 (the south one in their observation) and presented northeast to southwest distribution. In the north of G075.76+00.33, the UCHII region 075.78+00.34 was mapped by Wood & Churchwell (1989). This UCHII region was mapped H42 α emission toward G075.76+00.33 observation in the present work (see figure 12). An east to west distribution of ortho-NH₂D was obtained in G075.76+00.33 (see figure 12). The H¹³CN 1-0 was also mapped in G075.76+00.33 (see figure 12), and it has a similar distribution to HCN 1-0 emission, which has been observed by Riffel & Lüdke (2010). The ortho-NH₂D emission is in the south of G075.76+00.33, away from the H42 α emission in G075.76+00.33.

3.5.13 G081.75+00.59

G081.75+00.59 (DR 21) is a giant star-forming complex in Cygnus X molecular cloud complex (Dickel, Dickel, & Wilson 1978; Kirby 2009). It had been mapped to a 4 pc length ridge by Herschel observations (Motte et al. 2007; Hennemann et al. 2012) and contains three OH 1665 MHz emissions regions DR 21M, DR 21OH and W 75S (Koley et al. 2021). With IRAM observation, Christensen et al. (2023) reported integrated column density map of NH₂D, DCN, DNC and DCO⁺ toward Cygnus-X. In our previous work, this target has been detected the strongest velocity integrated intensity of para-NH₂D $1_{11}^a - 1_{01}^s$ at 110.1535 GHz with IRAM-30m and the highest deuterated fraction of NH₃ ($D_{\text{frac}}=0.044$) (Li et al. 2022). In the present work, we mapped DR 21 (OH) and W 75S in DR 21 and we describe them separately in the following two parts.

W75S-FIR1, W75S-FIR2 and W75S-FIR3 embedded several massive YSOs in W 75S (Harvey et al. 1986; Motte et al. 2007). Near W75S-FIR2 (20^h39^m02.4^s 42°24'59"), the strongest ortho-NH₂D emission was detected in the present work. In W 75S, the distribution of ortho-NH₂D is slightly similar to H¹³CN 1-0 (see figure 13).

DR 21OH contains several high mass protostars (Mangum, Wooten, & Mundy 1991). It is younger than DR 21M because it was undetected in the radio continuum emission (Davis et al. 2007). In the present work, we only obtained the north part in DR 21OH. The

ortho-NH₂D and H¹³CN 1-0 emissions are strong in this region (see figure 13). The H¹³CN 1-0 presents a strong peak in the southernmost toward our map and ortho-NH₂D offset the H¹³CN peak.

3.5.14 G081.87+00.78

G081.87+00.78 (W 75N) is a massive star-forming region in Cygnus X molecular cloud complex and it is in the north of G081.75+00.59 (Dickel, Dickel, & Wilson 1978; Persi, Tapia, & Smith 2006). This source contains a large-scale high-velocity molecular outflow (Shepherd, Testi, & Stark 2003) and a B-type YSO (Shepherd, Kurtz, & Testi 2004). In the present work, the ortho-NH₂D and H¹³CN 1-0 emission were obtained in G081.87+00.78, while H42 α was not detected (see figure 14). In G081.87+00.78, the ortho-NH₂D is oriented northwest-southeast and deviates the H¹³CN 1-0 peak.

3.5.15 G109.87+02.11

G109.87+02.11 (Cep A) is an active massive star-forming region, and it has been detected in several YSOs (Hughes & Wouterloot 1984). The brightest radio source in G109.87+02.11 is HW2 (where locates at (0'', 0'') in our maps), associated with an early-B spectral type zero-age main-sequence (ZAMS) star (Hughes & Wouterloot 1984). With IRAM 30-m observations, Li et al. (2017) observed strong ortho-NH₂D emission in the northeast of G109.87+02.11. As is shown in figure 15, the H¹³CN 1-0 and strong ortho-NH₂D emission were detected in G109.87+02.11. The distribution of ortho-NH₂D is presented in the northeast of G109.87+02.11, and it is similar to the result of Li et al. (2017). However, the ortho-NH₂D is dislocation with the strongest H¹³CN 1-0 emission. The strongest H¹³CN 1-0 emission is situated in proximity to HW2, and the ortho-NH₂D emissions appearing to be isolated by HW2. Besides, in this target, the strong ortho-NH₂D was detected in the northeast of G109.87+02.11 and H¹³CN was detected relatively weakly.

3.5.16 G111.54+00.77

G111.54+00.77 (NGC 7538) is a massive star-forming region which locates in a giant molecular cloud complex (Ungerechts, Umbanhowar, & Thaddeus 2000). With Herschel observation, Fallscheer et al. (2013) reported that G111.54+00.77 has several high-mass dense clumps candidates which may produce several intermediate- to high-mass stars in the future. A young O star with 25 M_⊙ embedded in NGC 7538 IRS 1 has been observed with a widely distributed molecular outflow (Qiu, Zhang, & Menten 2011). In G111.54+00.77, the widely distributed ortho-NH₂D and H¹³CN 1-0 distribution were detected (see figure 16), and H42 α emission was detected in the north where is NGC 7538 IRS 1. A small part of ortho-NH₂D emission is near to the H42 α emission while a large part appears in the south of G111.54+00.77. In the west of G111.54+00.77, the ortho-NH₂D emission is strong while H¹³CN 1-0 emission is weak.

3.5.17 G121.29+00.65

Toward SMA observations, Juárez et al. (2019) reported that G121.29+00.65 (L 1287) have a high fragmentation level and a bipolar outflow is oriented northeast to southwest direction. G121.29+00.65 have been detected 6.7 GHz CH₃OH, implying that there is forming a massive star (Rygl et al. 2010). In G121.29+00.65, the distribution of H¹³CN 1-0 was obtained (see figure 17), similar to the distribution of HCN 1-0 which is reported by Yang et al.

(1991). The distribution of ortho-NH₂D is perpendicular to H¹³CN 1-0 and the widely distributed ortho-NH₂D is oriented northwest to the southeast. The distribution of ortho-NH₂D is also perpendicular to the outflow reported in Juárez et al. (2019).

3.5.18 G188.94+00.88

It was reported that G188.94+00.88 (S 252) includes two massive protostars and is near to the Sh 2-247 which is a complex of HII region and OB stars (Minier et al. 2005). Several very weak ortho-NH₂D fragments were detected in G188.94+00.88 (see figure 18). These ortho-NH₂D emissions are marginally detected in this target. Similar to G005.88-00.39, the spatial structure might also not be distinguished in G188.94+00.88 due to the beam size. The main ortho-NH₂D emission region is presented in the south of H¹³CN 1-0 distribution. In G188.94+00.88, H42 α was not detected.

4 DISCUSSION

4.1 Spatial distribution of ortho-NH₂D and the dense molecular gas

As shown in figure 1-18 and Section 3.5, most of the targets manifest that the NH₂D emission deviates the H¹³CN 1-0 in the present work, such as G109.87+00.78 (see Figure 15). Moreover, five sources, G031.28+00.06, G035.19-00.74, G081.87+00.78, G109.87+02.11 and G121.29+00.65 (see Figure 5, Figure 7, Figure 14, Figure 15 and Figure 17, respectively), present that the strong NH₂D emissions appear in some regions where the H¹³CN 1-0 emission is weak or even is marginally detected.

In four sources, G011.91-00.61, G023.44-00.18, G034.39+00.22 and G049.48-00.38, the distribution of strong ortho-NH₂D emission is similar to H¹³CN 1-0 (see Figure 2, Figure 4, Figure 6 and Figure 11, respectively). However, the ortho-NH₂D is not detected asymmetrically distributed spatial structure in G011.91-00.61, G023.44-00.18, G034.39+00.22 and G049.48-00.38. Their substructure is unresolved. Therefore, we can not confirm whether NH₂D emission and H¹³CN 1-0 have similar distributions in these sources or not.

Without asymmetrically distributed spatial structures detected and unresolved sources, only G081.75+00.59 presents a relatively similar distribution between NH₂D and H¹³CN 1-0. There may exist contingencies in this distribution.

As described in Section 3.3, H¹³CN 1-0 is used as a dense gas tracer (Gao & Solomon 2004; Wu et al. 2010; Vasyunina et al. 2011) in the present work to analyze the distribution of NH₂D and dense gas in massive star-forming late stage.

Crapsi et al. (2007) performed observations of para-NH₂D 1₁₁^a – 1₀₁^s at 110.1535 GHz toward low-mass starless core L 1544 with PdBI and they found that NH₂D intensity peaks were at 1.2 mm continuum dust peak. Therefore, they suggested that NH₂D is a good tracer of the high density gas in the low-mass starless core. However, toward the gas-phase model, Roberts & Millar (2000b) simulated that gas density seems to have no effect on D_{frac}(NH₃).

In present work, NH₂D seems to be enhanced in G031.28+00.06, G035.19-00.74, G081.87+00.78, G109.87+02.11 and G121.29+00.65, at relatively low gas density part (see Figure 5, Figure 7, Figure 14, Figure 15 and Figure 17, respectively). Therefore, such results indicate that the gas density may not be an important physical parameter to influence the abundance of NH₂D, which is opposite to that of Crapsi et al. (2007) and agrees with the gas-phase model of Roberts & Millar (2000b). Compared with other physical

parameters (such as temperature), the gas density might not be the important physical parameter to affect the abundance of NH₂D in the late-stage massive star-forming regions. But without any information of NH₃, we can not confirm that the $D_{\text{frac}}(\text{NH}_3)$ is affected by dense gas. More detail should be obtained with the information of NH₃.

4.2 Spatial distribution of ortho-NH₂D and massive star formation

To analyze whether NH₂D is affected by the formed massive young stellar objects or not, we compare the distribution between ortho-NH₂D and H42 α . In the present work, ortho-NH₂D and HII regions present a different distribution in most targets. Both ortho-NH₂D and H42 α emissions were detected in nine targets. In five sources, G015.03-00.67, G031.28+00.06, G035.20-01.73, G075.76+00.33 and G111.54+00.77, the NH₂D emission are away from HII regions (see Figure 3, Figure 5, Figure 8, Figure 12 and Figure 16, respectively). In these five HII regions, the NH₂D may be depleted during the massive stars forming.

For G049.48-00.36 and G049.48-00.38, the relatively strong ortho-NH₂D emission was detected in HII regions (see Figure 10 and Figure 11). The structure in W 51 is complex (Scoville & Solomon 1973), we can not confirm if that the ortho-NH₂D and H42 α emission come from the same structure. But it is obvious that ortho-NH₂D emission is away from H42 α emission, especially the strong H42 α emission and the center of the HII region.

The ortho-NH₂D presents two structures in G011.91-00.61 (see Figure 2). One is the northeast structure which is similar to the distribution of H42 α emission; another is the southwest structure without H42 α emission. However, the ortho-NH₂D emissions in the southwest structure are stronger and more extensive than emissions in the northeast structure. The reason may be that the massive star-forming stage in the northeast part is later than the southwest structure, and as a result, NH₂D in the northeast part is much more depleted than NH₂D in the southwest part.

In cold molecular gas, there is an active process of deuterated molecules forming (Caselli & Ceccarelli 2012). And during this process, several neutral species are frozen-out onto dust grains and molecules are deuterated on the surface of dust grains (Caselli & Ceccarelli 2012). Moreover, according to the simulation, Caselli et al. (2008) suggested that the deuterium fractionation of H₃⁺ (which means the abundance ratio of H₃⁺ to H₂D⁺) dropped rapidly when the gas kinetic temperature is above ~ 15 K. The formation process of NH₂D is related to H₂D⁺ (Emprechtinger et al. 2009). It may indicate that the $D_{\text{frac}}(\text{NH}_3)$ decreases with temperature increasing when the temperature is relatively high. Besides, with PdBI observation toward the massive star-forming region IRAS 20293+3952, Busquet et al. (2010) reported that they found strong NH₂D emission in starless cores and did not detect NH₂D near YSOs. Therefore, according to previous research of observation and theory (e.g. Caselli et al. 2008; Emprechtinger et al. 2009; Busquet et al. 2010; Caselli & Ceccarelli 2012), the abundance of NH₂D should decrease with the evolution of massive star formation.

Without H42 α detected, these nine sources present both strong and weak NH₂D emission. In two sources, G037.43+01.51 and G188.94+00.88, the velocity integrated intensity of ortho-NH₂D is lower than 1 K km/s (see Figure 9 and Figure 18). In G037.43+01.51, the NH₃ column density has been derived with VLA observation (Lu et al. 2014). Compared with other sources, this target presents low column density, such as G034.39+00.22 whose column density is one order of magnitude higher than G037.43+01.51 (Lu et al. 2014). Similarly, the NH₃ column density of G188.94+00.88 is also lower

than other sources, such as G081.75+00.59 whose column density is one order of magnitude higher than G188.94+00.88 with Effelsberg observation (Jijina, Myers, & Adams 1999). With low NH₃ column density, the NH₂D might generate relatively less in these two sources.

The NH₂D seems to be depleted near the HII regions which indicates a later evolution stage. Furthermore, in the region without H42 α emission, the strong ortho-NH₂D emission is detected. Therefore, combining with previous researches (e.g. Caselli et al. 2008; Emprechtinger et al. 2009; Busquet et al. 2010; Caselli & Ceccarelli 2012), we suggest that the abundance of NH₂D may be affected by the evolution of massive star formation.

4.3 NH₂D enhancement

With the Green Bank Telescope and the K-Band Focal Plane Array observation, Urquhart et al. (2015) have mapped the NH₃ (1,1) and NH₃ (2,2) inversion emission toward 66 massive star-forming regions, identified by the Red Midcourse Space Experiment Source survey (Lumsden et al. 2013). These 66 massive star-forming regions include several of our targets, such as G035.19-00.74 (see figure 20). In G035.19-00.74, strong NH₂D emissions present a northwest to southeast distribution, while the northwest and the southeast regions present weak H¹³CN 1-0 emission (see figure 7), these regions might be devoid of dense molecular gases. However, in the weak H¹³CN 1-0 region, NH₃ (1,1) and NH₃ (2,2) were detected. Therefore, the molecular gases that exist in these regions and their density is relatively low.

The obvious NH₂D enrichment is presented in the southeast and northwest of G035.19-00.74. In particular, in the northwest of G035.19-00.74, the very high deuterium fractionation of NH₃ is detected. Compared with the H¹³CN emission in G035.19-00.74, the deuterium fractionation of NH₃ is either not affected by gas density. Moreover, combining with the ammonia data, we could obtain the distribution of the deuterium fractionation in the following work.

5 SUMMARY AND CONCLUSION REMARKS

Using of the IRAM-30m, we carried the ortho-NH₂D $1_{11}^s - 1_{01}^a$ at 85.9263 GHz mapping toward a sample of 24 late stage massive star-forming. The ortho-NH₂D $1_{11}^s - 1_{01}^a$ at 85.9263 GHz was detected in 18 targets. H¹³CN 1-0 at 86.3387 GHz was also detected in these 18 targets, while H42 α at 85.6884 GHz was detected in nine targets.

11 of 18 sources, present a different distribution between ortho-NH₂D $1_{11}^s - 1_{01}^a$ and H¹³CN 1-0 with asymmetrically and resolvable distributed spatial structure. For the other 7 sources, no significant difference between these two lines can be found. This is mainly due to the limited spatial resolution and sensitivity.

Our main results include:

1. The ortho-NH₂D $1_{11}^s - 1_{01}^a$ emissions present a complex distribution, which is different from other molecule transitions, such as H¹³CN 1-0.
2. Most of the targets show the different distribution between ortho-NH₂D $1_{11}^s - 1_{01}^a$ and H¹³CN 1-0. Compared with other physical parameters (such as temperature), therefore, the dense gas (or gas density) may not be an important physical parameter to affect the NH₂D enhancement in these targets.
3. The ortho-NH₂D $1_{11}^s - 1_{01}^a$ emissions are away from the H42 α . Combining with previous researches (e.g. Caselli et al. 2008; Emprechtinger et al. 2009; Busquet et al. 2010; Caselli & Cecca-

relli 2012), the abundance of NH₂D may be affected during the massive star-forming.

ACKNOWLEDGEMENTS

This work is supported by the National Key R&D Program of China (No. 2022YFA1603101) and the National Natural Science Foundation of China (NSFC, Grant No. 12173067). This study is based on observations carried out under project numbers 042-19, 147-19, and 127-20 with the IRAM 30-m telescope. IRAM is supported by INSU/CNRS (France), MPG (Germany) and IGN (Spain).

DATA AVAILABILITY

The original data observed with IRAM 30 meter can be accessed by IRAM archive system at <https://www.iram-institute.org/EN/content-page-386-7-386-0-0-0.html>. If anyone is interested in the reduced data presented in this paper, please contact Junzhi Wang at junzhiwang@gxu.edu.cn.

REFERENCES

- Acord J. M., Churchwell E., Wood D. O. S., 1998, *ApJL*, 495, L107. doi:10.1086/311230
- Beuther H., Schilke P., Menten K. M., Motte F., Sridharan T. K., Wyrowski F., 2002, *ApJ*, 566, 945. doi:10.1086/338334
- Brown P. D., Millar T. J., 1989, *MNRAS*, 240, 25P. doi:10.1093/mnras/240.1.25P
- Busquet G., Palau A., Estalella R., Girart J. M., Sánchez-Monge Á., Viti S., Ho P. T. P., et al., 2010, *A&A*, 517, L6. doi:10.1051/0004-6361/201014866
- Caselli P., Vastel C., Ceccarelli C., van der Tak F. F. S., Crapsi A., Bacmann A., 2008, *A&A*, 492, 703. doi:10.1051/0004-6361:20079009
- Caselli P., Ceccarelli C., 2012, *A&ARv*, 20, 56. doi:10.1007/s00159-012-0056-x
- Cazaux S., Tielens A. G. G. M., Ceccarelli C., Castets A., Wakelam V., Caux E., Parise B., et al., 2003, *ApJL*, 593, L51. doi:10.1086/378038
- Ceccarelli C., Caselli P., Bockelée-Morvan D., Mousis O., Pizzarello S., Robert F., Semenov D., 2014, *prpl.conf*, 859. doi:10.2458/azu_uapress_9780816531240-ch037
- Crapsi A., Caselli P., Walmsley M. C., Tafalla M., 2007, *A&A*, 470, 221. doi:10.1051/0004-6361:20077613
- Christensen I. B., Wyrowski F., Menten K. M., Beuther H., Cascade Team, 2023, *pcsf.conf*, 253
- Cox P., Guesten R., Henkel C., 1987, *A&A*, 181, L19
- Davis C. J., Kumar M. S. N., Sandell G., Froebrich D., Smith M. D., Currie M. J., 2007, *MNRAS*, 374, 29. doi:10.1111/j.1365-2966.2006.11163.x
- Dent W. R. F., Little L. T., White G. J., 1984, *MNRAS*, 210, 173. doi:10.1093/mnras/210.1.173
- Dickel J. R., Dickel H. R., Wilson W. J., 1978, *ApJ*, 223, 840. doi:10.1086/156317
- Emprechtinger M., Caselli P., Volgenau N. H., Stutzki J., Wiedner M. C., 2009, *A&A*, 493, 89. doi:10.1051/0004-6361:200810324
- Evans A. S., Solomon P. M., Tacconi L. J., Vavilkin T., Downes D., 2006, *AJ*, 132, 2398. doi:10.1086/508416
- Fallscheer C., Reid M. A., Di Francesco J., Martin P. G., Hill T., Hennemann M., Nguyen-Luong Q., et al., 2013, *ApJ*, 773, 102. doi:10.1088/0004-637X/773/2/102
- Fedoseev G., Ioppolo S., Linnartz H., 2015, *MNRAS*, 446, 449. doi:10.1093/mnras/stu1852
- Feldt M., Puga E., Lenzen R., Henning T., Brandner W., Stecklum B., Lagrange A.-M., et al., 2003, *ApJL*, 599, L91. doi:10.1086/381174
- Gao Y., Solomon P. M., 2004, *ApJ*, 606, 271. doi:10.1086/382999
- Gibb A. G., Hoare M. G., Little L. T., Wright M. C. H., 2003, *MNRAS*, 339, 1011. doi:10.1046/j.1365-8711.2003.06251.x
- Ginsburg A., Bressert E., Bally J., Battersby C., 2012, *ApJL*, 758, L29. doi:10.1088/2041-8205/758/2/L29
- Gong Y., Henkel C., Thorwirth S., Spezzano S., Menten K. M., Walmsley C. M., Wyrowski F., et al., 2015, *A&A*, 581, A48. doi:10.1051/0004-6361/201526275
- Harju J., Daniel F., Sipilä O., Caselli P., Pineda J. E., Friesen R. K., Punanova A., et al., 2017, *A&A*, 600, A61. doi:10.1051/0004-6361/201628463
- Harvey P. M., Joy M., Lester D. F., Wilking B. A., 1986, *ApJ*, 300, 737. doi:10.1086/163848
- Harvey P. M., Forveille T., 1988, *A&A*, 197, L19
- Hatchell J., 2003, *A&A*, 403, L25. doi:10.1051/0004-6361:20030297
- Hennemann M., Motte F., Schneider N., Didelon P., Hill T., Arzoumanian D., Bontemps S., et al., 2012, *A&A*, 543, L3. doi:10.1051/0004-6361/201219429
- Herbst E., 1982, *A&A*, 111, 76
- Ho P. T. P., Townes C. H., 1983, *ARA&A*, 21, 239. doi:10.1146/annurev.aa.21.090183.001323
- Hughes V. A., Wouterloot J. G. A., 1984, *ApJ*, 276, 204. doi:10.1086/161603
- Ilee J. D., Cyganowski C. J., Brogan C. L., Hunter T. R., Forgan D. H., Harworth T. J., Clarke C. J., et al., 2018, *ApJL*, 869, L24. doi:10.3847/2041-8213/aaeffc
- Jijina J., Myers P. C., Adams F. C., 1999, *ApJS*, 125, 161. doi:10.1086/313268
- Juárez C., Liu H. B., Girart J. M., Palau A., Busquet G., Galván-Madrid R., Hirano N., et al., 2019, *A&A*, 621, A140. doi:10.1051/0004-6361/201834173
- Kirby L., 2009, *ApJ*, 694, 1056. doi:10.1088/0004-637X/694/2/1056
- Koley A., Roy N., Menten K. M., Jacob A. M., Pillai T. G. S., Rugel M. R., 2021, *MNRAS*, 501, 4825. doi:10.1093/mnras/staa3898
- Lada C. J., 1976, *ApJS*, 32, 603. doi:10.1086/190409
- Lada E. A., Bally J., Stark A. A., 1991, *ApJ*, 368, 432. doi:10.1086/169708
- Li S., Wang J., Zhang Z.-Y., Fang M., Li J., Zhang J., Fan J., et al., 2017, *MNRAS*, 466, 248. doi:10.1093/mnras/stw3076
- Li Y., Wang J., Li J., Liu S., Luo Q., 2022, *MNRAS*, 512, 4934. doi:10.1093/mnras/stab3186
- Lim W., De Buizer J. M., Radomski J. T., 2020, *ApJ*, 888, 98. doi:10.3847/1538-4357/ab5fd0
- Linsky J. L., Diplas A., Wood B. E., Brown A., Ayres T. R., Savage B. D., 1995, *ApJ*, 451, 335. doi:10.1086/176223
- Lis D. C., Gerin M., Phillips T. G., Motte F., 2002, *ApJ*, 569, 322. doi:10.1086/339232
- Lu X., Zhang Q., Liu H. B., Wang J., Gu Q., 2014, *ApJ*, 790, 84. doi:10.1088/0004-637X/790/2/84
- Lumsden S. L., Hoare M. G., Urquhart J. S., Oudmaijer R. D., Davies B., Mottram J. C., Cooper H. D. B., et al., 2013, *ApJS*, 208, 11. doi:10.1088/0067-0049/208/1/11
- Mangum J. G., Wootten A., Mundy L. G., 1991, *ApJ*, 378, 576. doi:10.1086/170459
- Mills E. A. C., Corby J., Clements A. R., Butterfield N., Jones P. A., Cunningham M. R., Ott J., 2018, *ApJ*, 869, 121. doi:10.3847/1538-4357/aaed3f
- Minier V., Burton M. G., Hill T., Pestalozzi M. R., Purcell C. R., Garay G., Walsh A. J., et al., 2005, *A&A*, 429, 945. doi:10.1051/0004-6361:20041137
- Miralles M. P., Rodríguez L. F., Scalise E., 1994, *ApJS*, 92, 173. doi:10.1086/191965
- Motte F., Bontemps S., Schilke P., Schneider N., Menten K. M., Broguière D., 2007, *A&A*, 476, 1243. doi:10.1051/0004-6361:20077843
- Müller H. S. P., Thorwirth S., Roth D. A., Winnewisser G., 2001, *A&A*, 370, L49. doi:10.1051/0004-6361:20010367
- Müller H. S. P., Schlöder F., Stutzki J., Winnewisser G., 2005, *JMoSt*, 742, 215. doi:10.1016/j.molstruc.2005.01.027
- Neill J. L., Crockett N. R., Bergin E. A., Pearson J. C., Xu L.-H., 2013, *ApJ*, 777, 85. doi:10.1088/0004-637X/777/2/85
- Nguyen Luong Q., Motte F., Schuller F., Schneider N., Bontemps S., Schilke P., Menten K. M., et al., 2011, *A&A*, 529, A41. doi:10.1051/0004-6361/201016271
- Oliveira C. M., Hébrard G., Howk J. C., Kruk J. W., Chayer P., Moos H. W.,

- 2003, ApJ, 587, 235. doi:10.1086/368019
- Pillai T., Kauffmann J., Wyrowski F., Hatchell J., Gibb A. G., Thompson M. A., 2011, A&A, 530, A118. doi:10.1051/0004-6361/201015899
- Persi P., Tapia M., Smith H. A., 2006, A&A, 445, 971. doi:10.1051/0004-6361:20053251
- Peters T., Longmore S. N., Dullemond C. P., 2012, MNRAS, 425, 2352. doi:10.1111/j.1365-2966.2012.21676.x
- Povich M. S., Churchwell E., Bieging J. H., Kang M., Whitney B. A., Brogan C. L., Kulesa C. A., et al., 2009, ApJ, 696, 1278. doi:10.1088/0004-637X/696/2/1278
- Qiu K., Zhang Q., Menten K. M., 2011, ApJ, 728, 6. doi:10.1088/0004-637X/728/1/6
- Rathborne J. M., Jackson J. M., Simon R., 2006, ApJ, 641, 389. doi:10.1086/500423
- Reid M. J., Menten K. M., Brunthaler A., Zheng X. W., Dame T. M., Xu Y., Wu Y., et al., 2014, ApJ, 783, 130. doi:10.1088/0004-637X/783/2/130
- Ren J. Z., Liu T., Wu Y., Li L., 2011, MNRAS, 415, L49. doi:10.1111/j.1745-3933.2011.01076.x
- Riffel R. A., Lüdke E., 2010, MNRAS, 404, 1449. doi:10.1111/j.1365-2966.2010.16355.x
- Rivilla V. M., Colzi L., Fontani F., Melosso M., Caselli P., Biz-zocchi L., Tamassia F., et al., 2020, MNRAS, 496, 1990. doi:10.1093/mnras/staa1616
- Roberts H., Millar T. J., 2000, A&A, 361, 388
- Roberts H., Millar T. J., 2000, A&A, 364, 780
- Rodgers S. D., Charnley S. B., 2001, ApJ, 553, 613. doi:10.1086/320987
- Rygl K. L. J., Brunthaler A., Reid M. J., Menten K. M., van Langevelde H. J., Xu Y., 2010, A&A, 511, A2. doi:10.1051/0004-6361/200913135
- Rygl K. L. J., Goedhart S., Polychroni D., Wyrowski F., Motte F., Elia D., Nguyen-Luong Q., et al., 2014, MNRAS, 440, 427. doi:10.1093/mnras/stu300
- Tiné S., Roueff E., Falgarone E., Gerin M., Pineau des Forêts G., 2000, A&A, 356, 1039
- Shah R. Y., Wootten A., 2001, ApJ, 554, 933. doi:10.1086/321396
- Shepherd D. S., Testi L., Stark D. P., 2003, ApJ, 584, 882. doi:10.1086/345743
- Shepherd D. S., Kurtz S. E., Testi L., 2004, ApJ, 601, 952. doi:10.1086/380633
- Scoville N. Z., Solomon P. M., 1973, ApJ, 180, 31. doi:10.1086/151940
- Turner B. E., 1990, ApJL, 362, L29. doi:10.1086/185840
- Ungerechts H., Umbanhowar P., Thaddeus P., 2000, ApJ, 537, 221. doi:10.1086/308992
- Urquhart J. S., Figura C. C., Moore T. J. T., Csengeri T., Lumsden S. L., Pillai T., Thompson M. A., et al., 2015, MNRAS, 452, 4029. doi:10.1093/mnras/stv1514
- Vastel C., Mookerjea B., Pety J., Gerin M., 2017, A&A, 597, A45. doi:10.1051/0004-6361/201629289
- Vasyunina T., Linz H., Henning T., Zinchenko I., Beuther H., Voronkov M., 2011, A&A, 527, A88. doi:10.1051/0004-6361/201014974
- Walsh A. J., Burton M. G., Hyland A. R., Robinson G., 1998, MNRAS, 301, 640. doi:10.1046/j.1365-8711.1998.02014.x
- Wienen M., Wyrowski F., Walmsley C. M., Csengeri T., Pillai T., Gian-netti A., Menten K. M., 2021, A&A, 649, A21. doi:10.1051/0004-6361/201731208
- Wood D. O. S., Churchwell E., 1989, ApJS, 69, 831. doi:10.1086/191329
- Wu J., Evans N. J., Shirley Y. L., Knez C., 2010, ApJS, 188, 313. doi:10.1088/0067-0049/188/2/313
- Xu Y., Moscadelli L., Reid M. J., Menten K. M., Zhang B., Zheng X. W., Brunthaler A., 2011, ApJ, 733, 25. doi:10.1088/0004-637X/733/1/25
- Yang J., Umemoto T., Iwata T., Fukui Y., 1991, ApJ, 373, 137. doi:10.1086/170032
- Zahorec S., Jimenez-Serra I., Testi L., Immer K., Fontani F., Caselli P., Wang K., et al., 2021, A&A, 653, A45. doi:10.1051/0004-6361/201937012
- Zapata L. A., Ho P. T. P., Fernández-López M., Ccolque E. G., Rodríguez L. F., Reyes-Valdés J., Bally J., et al., 2020, ApJL, 902, L47. doi:10.3847/2041-8213/abbd3f
- Zhang C.-P., Li G.-X., Pillai T., Csengeri T., Wyrowski F., Menten K. M., Pestalozzi M. R., 2020, A&A, 638, A105. doi:10.1051/0004-6361/201936118

Table 1: Source List

| source name | RA(J2000) hh:mm:ss | DEC(J2000) dd:mm:ss | D _{GC} kpc | v _{LSR} km s ⁻¹ | Size |
|---------------|-----------------------|------------------------|------------------------|----------------------------------------|-----------|
| G005.88-00.39 | 18:00:30.31 | -24:04:04.50 | 5.3 | 9 | 2' × 2' |
| G009.62+00.19 | 18:06:14.66 | -20:31:31.70 | 3.3 | 2 | 2' × 2' |
| G011.49-014.8 | 18:16:22.13 | -19:41:27.20 | 7.1 | 11 | 2' × 2' |
| G011.91-00.61 | 18:13:59.72 | -18:53:50.30 | 5.1 | 37 | 3' × 3' |
| G012.80-00.20 | 18:14:14.23 | -17:55:40.50 | 5.5 | 34 | 4' × 4' |
| G015.03-00.67 | 18:20:22.01 | -16:12:11.30 | 6.4 | 22 | 4' × 4' |
| G023.44-00.18 | 18:34:39.29 | -08:31:25.40 | 3.7 | 97 | 2' × 2' |
| G031.28+00.06 | 18:48:12.39 | -01:26:30.70 | 5.2 | 109 | 2' × 2' |
| G034.39+00.22 | 18:53:19.00 | +01:24:50.80 | 7.1 | 57 | 2' × 2' |
| G035.19-00.74 | 18:58:13.05 | +01:40:35.70 | 6.6 | 30 | 2' × 2' |
| G035.20-01.73 | 19:01:45.54 | +01:13:32.50 | 5.9 | 42 | 3' × 2' |
| G043.16+00.01 | 19:10:13.41 | +09:06:12.80 | 7.6 | 10 | 2' × 2' |
| G037.43+01.51 | 18:54:14.35 | +04:41:41.70 | 6.9 | 41 | 2' × 2' |
| G049.48-00.36 | 19:23:39.82 | +14:31:05.00 | 6.3 | 56 | 2' × 2' |
| G049.48-00.38 | 19:23:43.87 | +14:30:29.50 | 6.3 | 58 | 2' × 2' |
| G075.76+00.33 | 20:21:41.09 | +37:25:29.30 | 8.2 | -9 | 2' × 2' |
| G081.75+00.59 | 20:39:01.99 | +42:24:59.30 | 8.2 | -3 | 2' × 3' |
| G081.87+00.78 | 20:38:36.43 | +42:37:34.80 | 8.2 | 7 | 2' × 2' |
| G109.87+02.11 | 22:56:18.10 | +62:01:49.50 | 8.6 | -7 | 2.5' × 2' |
| G111.54+00.77 | 23:13:45.36 | +61:28:10.60 | 9.6 | -57 | 2' × 4' |
| G121.29+00.65 | 00:36:47.35 | +63:29:02.20 | 8.8 | -23 | 2' × 2' |
| G133.94+01.06 | 02:27:03.82 | +61:52:25.20 | 9.8 | -47 | 2' × 2' |
| G188.94+00.88 | 06:08:53.35 | +21:38:28.70 | 10.4 | 8 | 2' × 2' |
| G192.60-00.04 | 06:12:54.02 | +17:59:47.3 | 9.9 | 6 | 2' × 2' |

Table 2: Parameters of ortho-NH₂D 1₁₁^S – 1₀₁^A hyperfine structure

| F''-F''' | frequency (MHz) | relative intensity |
|----------|-----------------|--------------------|
| 0-1 | 85924.7829 | 0.111 |
| 2-1 | 85925.7031 | 0.139 |
| 2-2 | 85926.2703 | 0.417 |
| 1-1 | 85926.3165 | 0.083 |
| 1-2 | 85926.8837 | 0.139 |
| 1-0 | 85927.7345 | 0.111 |

Table 3: NH₂D velocity integrated intensity

| Source | $\int T_{\text{mb}}(85.9 \text{ GHz})dv$ K km s ⁻¹ | $\int T_{\text{mb}}(110 \text{ GHz})dv$ K km s ⁻¹ | $\frac{\int T_{\text{mb}}(85.9\text{GHz})dv}{\int T_{\text{mb}}(110\text{GHz})dv}$ |
|---------------|------------------------------------------------------------------|-----------------------------------------------------------------|------------------------------------------------------------------------------------|
| G005.88-00.39 | 0.33±0.15 | 0.37±0.07 | 0.89±0.44 |
| G011.91-00.61 | 2.24±0.14 | 1.08±0.05 | 2.07±0.16 |
| G015.03-00.67 | ≤0.509 | ≤0.157 | ... |
| G023.44-00.18 | 1.52± 0.14 | 0.75±0.05 | 2.03±0.23 |
| G031.28+00.06 | ≤0.280 | 0.18±0.04 | ... |
| G034.39+00.22 | 5.11± 0.18 | 1.73±0.03 | 2.95±0.12 |
| G035.19-00.74 | 1.29±0.16 | 0.57±0.04 | 2.26±0.32 |
| G035.20-01.73 | 0.52±0.11 | 0.11±0.04 | 4.73±1.99 |
| G037.43+01.51 | 0.31±0.11 | 0.18±0.02 | 1.72±0.64 |
| G049.48-00.36 | 1.06±0.17 | 0.55±0.05 | 1.93±0.36 |
| G049.48-00.38 | 2.92±0.14 | 2.31±0.06 | 1.26±0.07 |
| G075.76+00.33 | ≤0.305 | ≤0.096 | ... |
| G081.75+00.59 | 5.98±0.07 | 4.10±0.03 | 1.45±0.02 |
| G081.87+00.78 | 0.41±0.14 | 0.31±0.03 | 1.32±0.47 |
| G109.87+02.11 | ≤0.472 | 0.08±0.02 | ... |
| G111.54+00.77 | ≤0.881 | 0.20±0.02 | ... |
| G121.29+00.65 | 1.59±0.14 | 0.91±0.02 | 1.75±0.16 |
| G188.94+00.88 | ≤0.257 | 0.14±0.02 | ... |

Table 4: NH₂D, H¹³CN and H42α distribution information

| source | $\int T_{\text{mb}}(\text{NH}_2\text{D})dv$ K km s ⁻¹ | NH ₂ D direction | obvious structure | similar with H ¹³ CN | detected H42α |
|---------------|---------------------------------------------------------------------|-----------------------------|-------------------|---------------------------------|---------------|
| G005.88-00.39 | 0.60±0.16 | | | | ✓ |
| G011.91-00.61 | 2.33±0.15 | northeast-southwest | ✓ | ✓ | ✓ |
| G015.03-00.67 | 1.11±0.18 | fragmentization | | | ✓ |
| G023.44-00.18 | 2.31±0.13 | disciform | ✓ | ✓ | |
| G031.28+00.06 | 0.86±0.11 | northeast-southwest | ✓ | | ✓ |
| G034.39+00.22 | 5.11±0.18 | north-south | ✓ | ✓ | |
| G035.19-00.74 | 3.05±0.11 | northwest-southeast | ✓ | | |
| G035.20-01.73 | 4.06±0.11 | west-east | ✓ | | ✓ |
| G037.43+01.51 | 0.60±0.11 | irregular | | | |
| G049.48-00.36 | 2.45±0.17 | complex structure | ✓ | | ✓ |
| G049.48-00.38 | 2.92±0.14 | complex structure | ✓ | ✓ | ✓ |
| G075.76+00.33 | 1.27±0.17 | west-east | ✓ | | ✓ |
| G081.75+00.59 | 6.95±0.14 | north-south | ✓ | ✓ | |
| G081.87+00.78 | 1.70±0.13 | northwest-southeast | ✓ | | |
| G109.87+02.11 | 2.51±0.17 | northeast-southwest | ✓ | | |
| G111.54+00.77 | 1.86±0.16 | complex structure | ✓ | | ✓ |
| G121.29+00.65 | 2.22±0.26 | northwest-southeast | ✓ | | |
| G188.94+00.88 | 0.86±0.16 | | | | |

This paper has been typeset from a $\text{\TeX}/\text{\LaTeX}$ file prepared by the author.

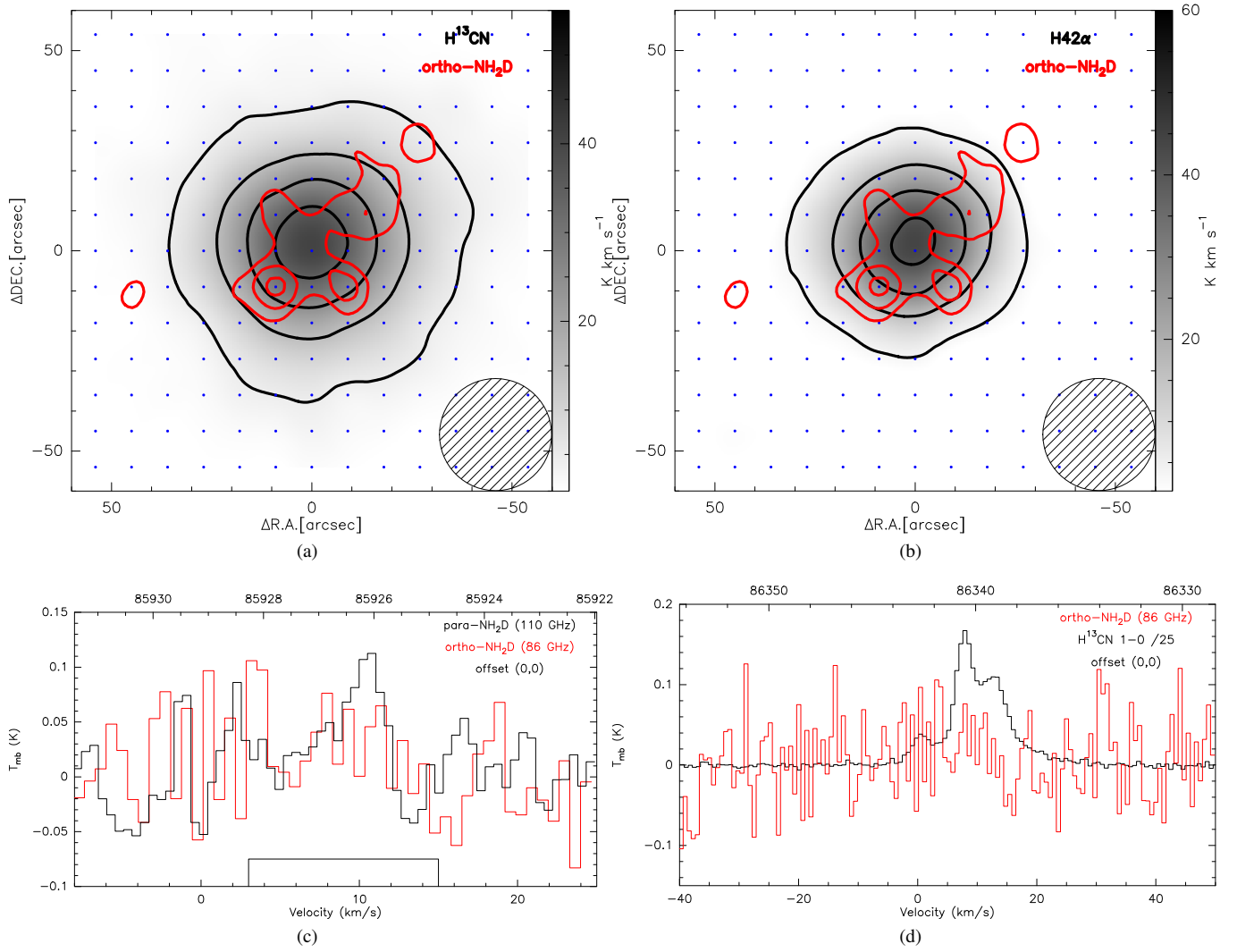


Figure 1. (a): NH₂D at 85.9263 GHz velocity integrated intensity contour (red contour) overlaid on H¹³CN 1-0 velocity integrated intensity image (gray scale and black contour) in G005.88-00.39. The contour levels start at 2σ in steps of 1σ for NH₂D, while the contour levels start at 18σ in steps of 36σ for H¹³CN 1-0. The gray scale starts at 3σ . (b): NH₂D at 85.9263 GHz velocity integrated intensity contour (red contour) overlaid on H42 α velocity integrated intensity image (Gray scale and black contour) in G005.88-00.39. The contour levels start at 2σ in steps of 1σ for NH₂D, while the contour levels start at 7σ in steps of 24σ for H42 α . The gray scale starts at 3σ . (c): Spectra of ortho-NH₂D at 85.9263 GHz and para-NH₂D at 110.1535 GHz in G005.88-00.39. The para-NH₂D was observed by IRAM-30m with position-switching mode. The red spectra is ortho-NH₂D and the black is para-NH₂D. The offset for two spectra is (0'',0''). (d): Spectra of ortho-NH₂D at 85.9263 GHz and H¹³CN 1-0 in G005.88-00.39. The red spectra is ortho-NH₂D and the black is H¹³CN 1-0. The offset for two spectra is (0'',0'').

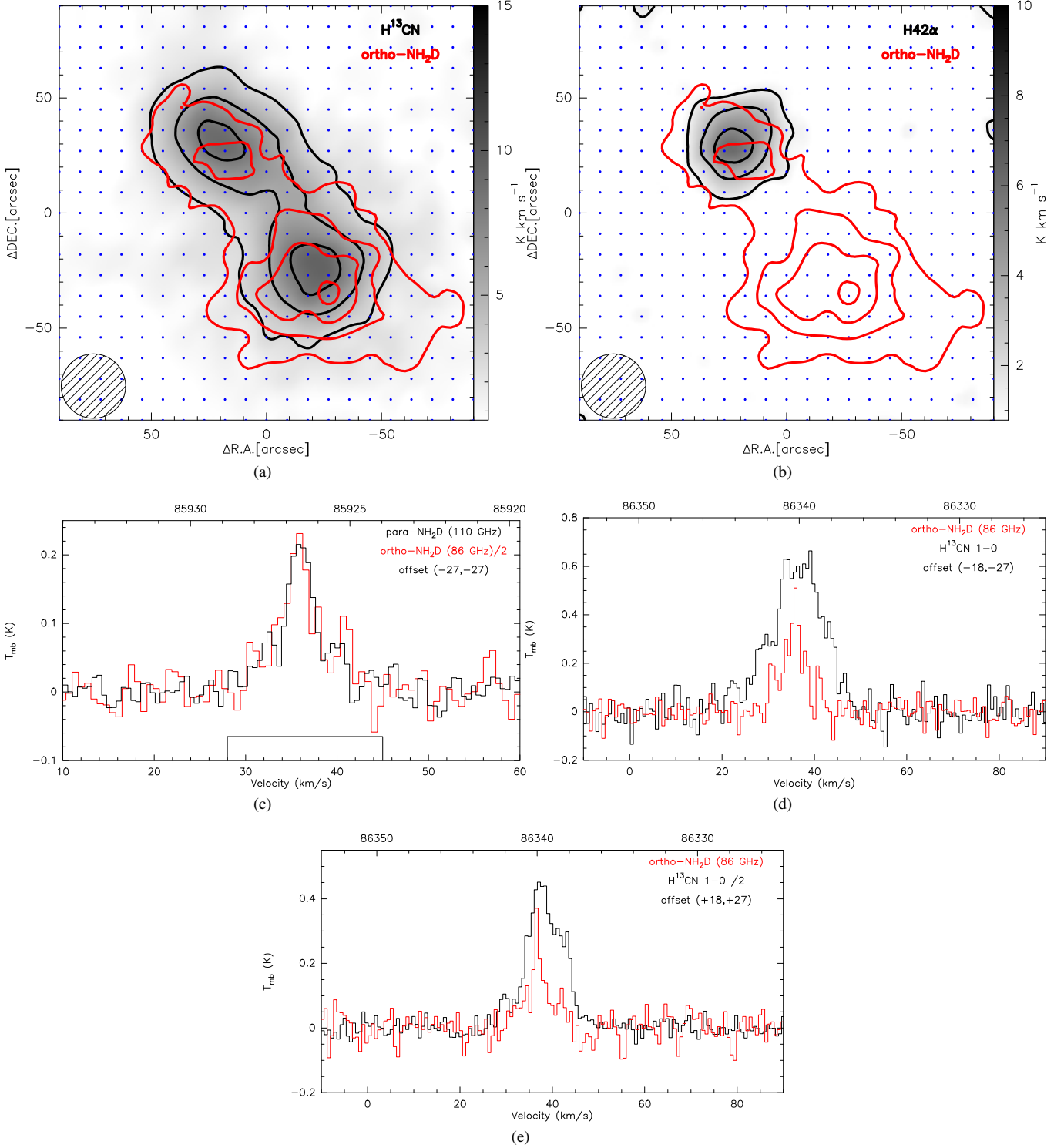


Figure 2. (a): NH₂D at 85.9263 GHz velocity integrated intensity contour (red contour) overlaid on H¹³CN 1-0 velocity integrated intensity image (Gray scale and black contour) in G011.91-00.61. The contour levels start at 5σ in steps of 4σ for NH₂D, while the contour levels start at 12σ in steps of 12σ for H¹³CN 1-0. The gray scale starts at 3σ. (b): NH₂D at 85.9263 GHz velocity integrated intensity contour (red contour) overlaid on H42α velocity integrated intensity image (Gray scale and black contour) in G011.91-00.61. The contour levels start at 5σ in steps of 4σ for NH₂D, while the contour levels start at 5σ in steps of 7σ for H42α. The gray scale starts at 3σ. (c): Spectra of ortho-NH₂D at 85.9263 GHz and para-NH₂D at 110.1535 GHz in G011.91-00.61. The para-NH₂D was observed by IRAM-30m with position-switching mode. The red spectra is ortho-NH₂D and the black is para-NH₂D. The offset for two spectra is (-27'', -27''). The black box in the picture indicates the range of flux integration of ortho-NH₂D at 85.9263 GHz. (d): Spectra of ortho-NH₂D at 85.9263 GHz and H¹³CN 1-0 in G011.91-00.61. The red spectra is ortho-NH₂D and the black is H¹³CN 1-0. The offset for two spectra is (-18'', -27''). (e): Spectra of ortho-NH₂D at 85.9263 GHz and H¹³CN 1-0 in G011.91-00.61. The red spectra is ortho-NH₂D and the black is H¹³CN 1-0. The offset for two spectra is (+18'', +27'').

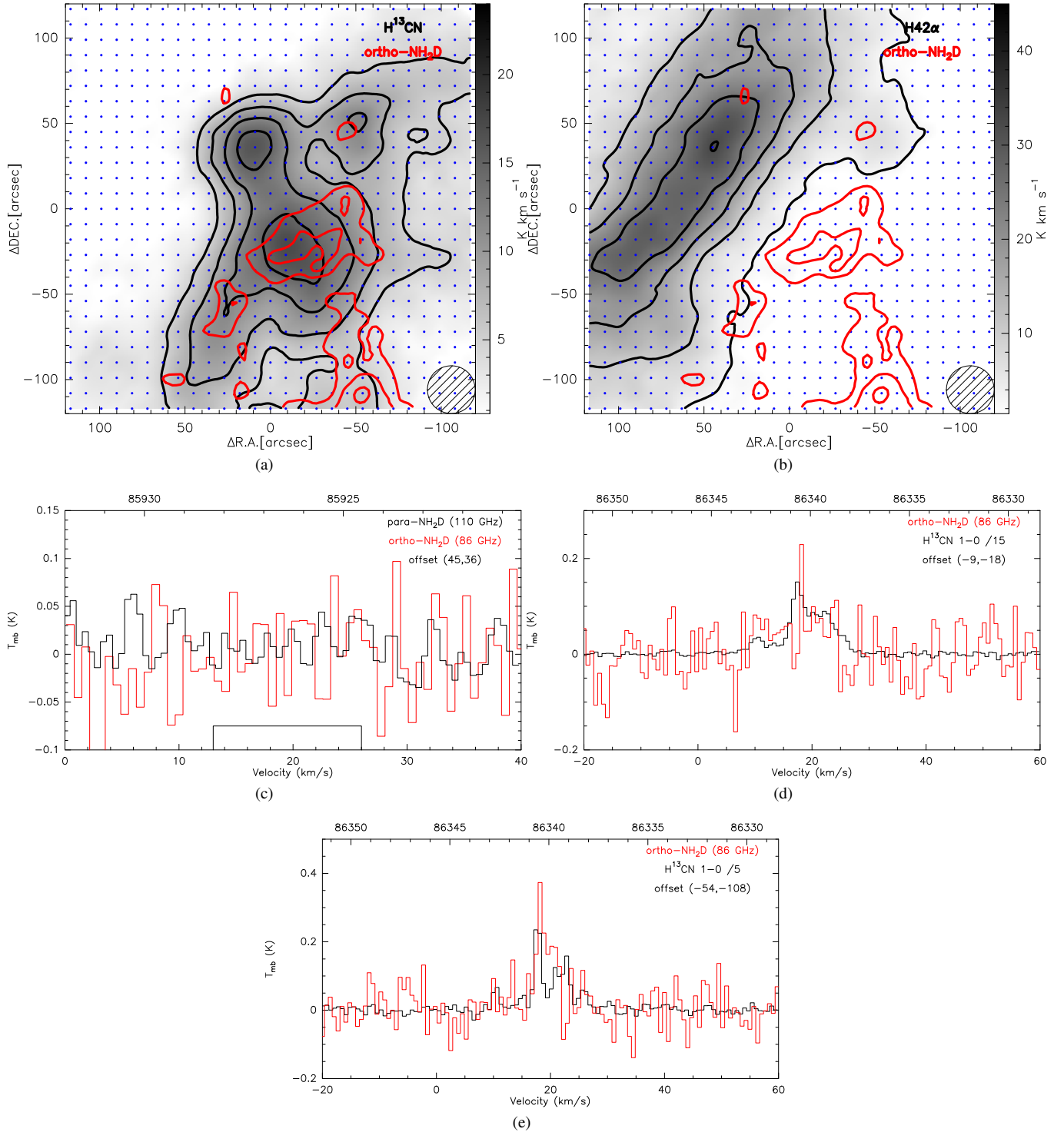


Figure 3. (a): NH_2D at 85.9263 GHz velocity integrated intensity contour (red contour) overlaid on H^{13}CN 1-0 velocity integrated intensity image (Gray scale and black contour) in G015.03-00.67. The contour levels start at 3σ in steps of 2σ for NH_2D , while the contour levels start at 18σ in steps of 12σ for H^{13}CN 1-0. The gray scale starts at 3σ . (b): NH_2D at 85.9263 GHz velocity integrated intensity contour (red contour) overlaid on $\text{H}42\alpha$ velocity integrated intensity image (Gray scale and black contour) in G015.03-00.67. The contour levels start at 3σ in steps of 2σ for NH_2D , while the contour levels start at 6σ in steps of 15σ for $\text{H}42\alpha$. The gray scale starts at 3σ . (c): Spectra of $\text{ortho-NH}_2\text{D}$ at 85.9263 GHz and $\text{para-NH}_2\text{D}$ at 110.1535 GHz in G015.03-00.67. The $\text{para-NH}_2\text{D}$ was observed by IRAM-30m with position-switching mode. The red spectra is $\text{ortho-NH}_2\text{D}$ and the black is $\text{para-NH}_2\text{D}$. The offset for two spectra is ($45''$, $36''$). The black box in the picture indicates the range of flux integration of $\text{ortho-NH}_2\text{D}$ at 85.9263 GHz. (d): Spectra of $\text{ortho-NH}_2\text{D}$ at 85.9263 GHz and H^{13}CN 1-0 in G015.03-00.67. The red spectra is $\text{ortho-NH}_2\text{D}$ and the black is H^{13}CN 1-0. The offset for two spectra is ($-9''$, $-18''$). (e): Spectra of $\text{ortho-NH}_2\text{D}$ at 85.9263 GHz and H^{13}CN 1-0 in G015.03-00.67. The red spectra is $\text{ortho-NH}_2\text{D}$ and the black is H^{13}CN 1-0. The offset for two spectra is ($-54''$, $-108''$).

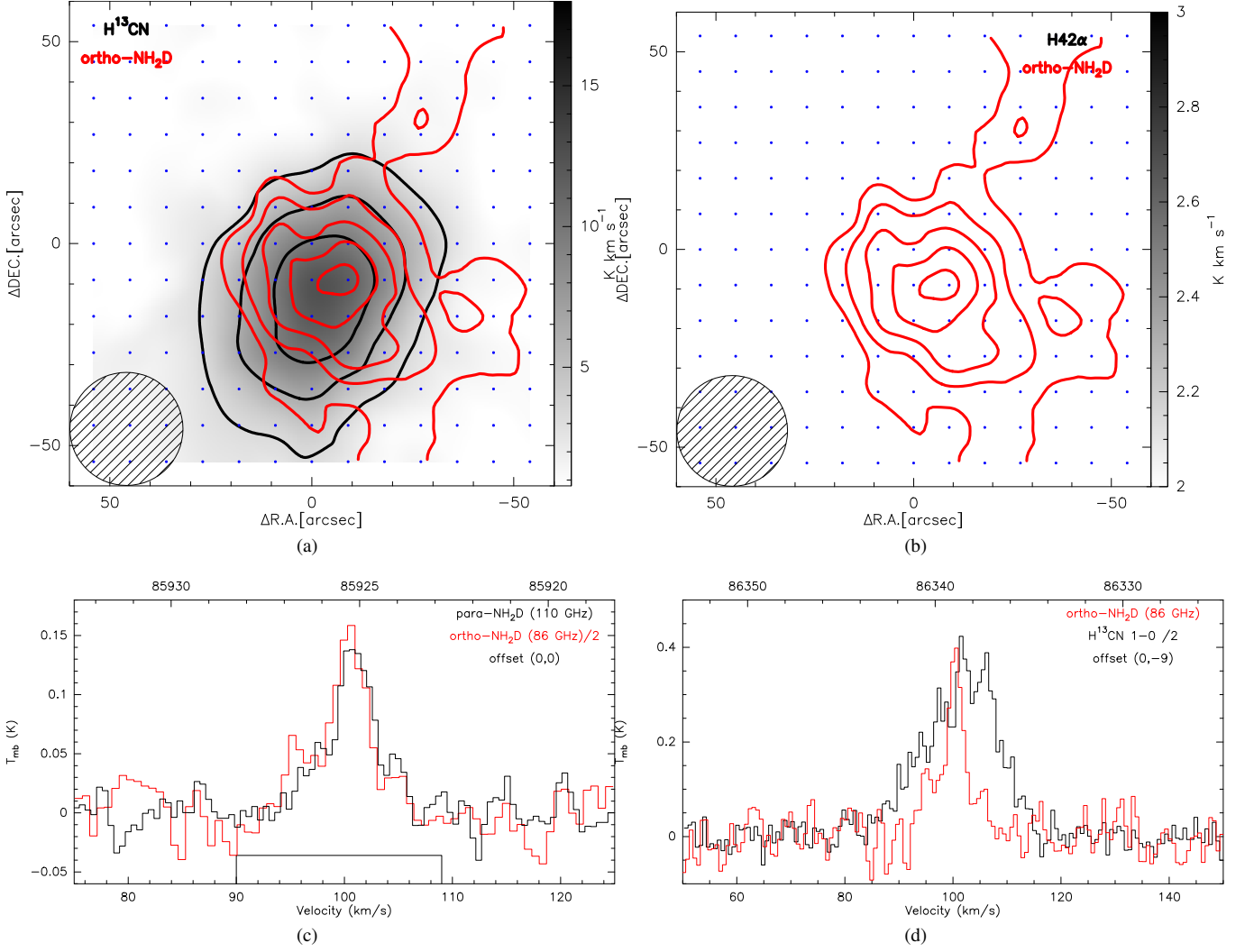


Figure 4. (a): NH₂D at 85.9263 GHz velocity integrated intensity contour (red contour) overlaid on H¹³CN 1-0 velocity integrated intensity image (Gray scale and black contour) in G023.44-00.18. The contour levels start at 5σ in steps of 3σ for NH₂D, while the contour levels start at 12σ in steps of 12σ for H¹³CN 1-0. The gray scale starts at 3σ . (b): NH₂D at 85.9263 GHz velocity integrated intensity contour (red contour) overlaid on H42α velocity integrated intensity image (Gray scale and black contour, while the H42α is not detected) in G023.44-00.18. The contour levels start at 5σ in steps of 3σ for NH₂D. (c): Spectra of ortho-NH₂D at 85.9263 GHz and para-NH₂D at 110.1535 GHz in G023.44-00.18. The para-NH₂D was observed by IRAM-30m with position-switching mode. The red spectra is ortho-NH₂D and the black is para-NH₂D. The offset for two spectra is (0'',0''). The black box in the picture indicates the range of flux integration of ortho-NH₂D at 85.9263 GHz. (d): Spectra of ortho-NH₂D at 85.9263 GHz and H¹³CN 1-0 in G023.44-00.18. The red spectra is ortho-NH₂D and the black is H¹³CN 1-0. The offset for two spectra is (0'',-9'').

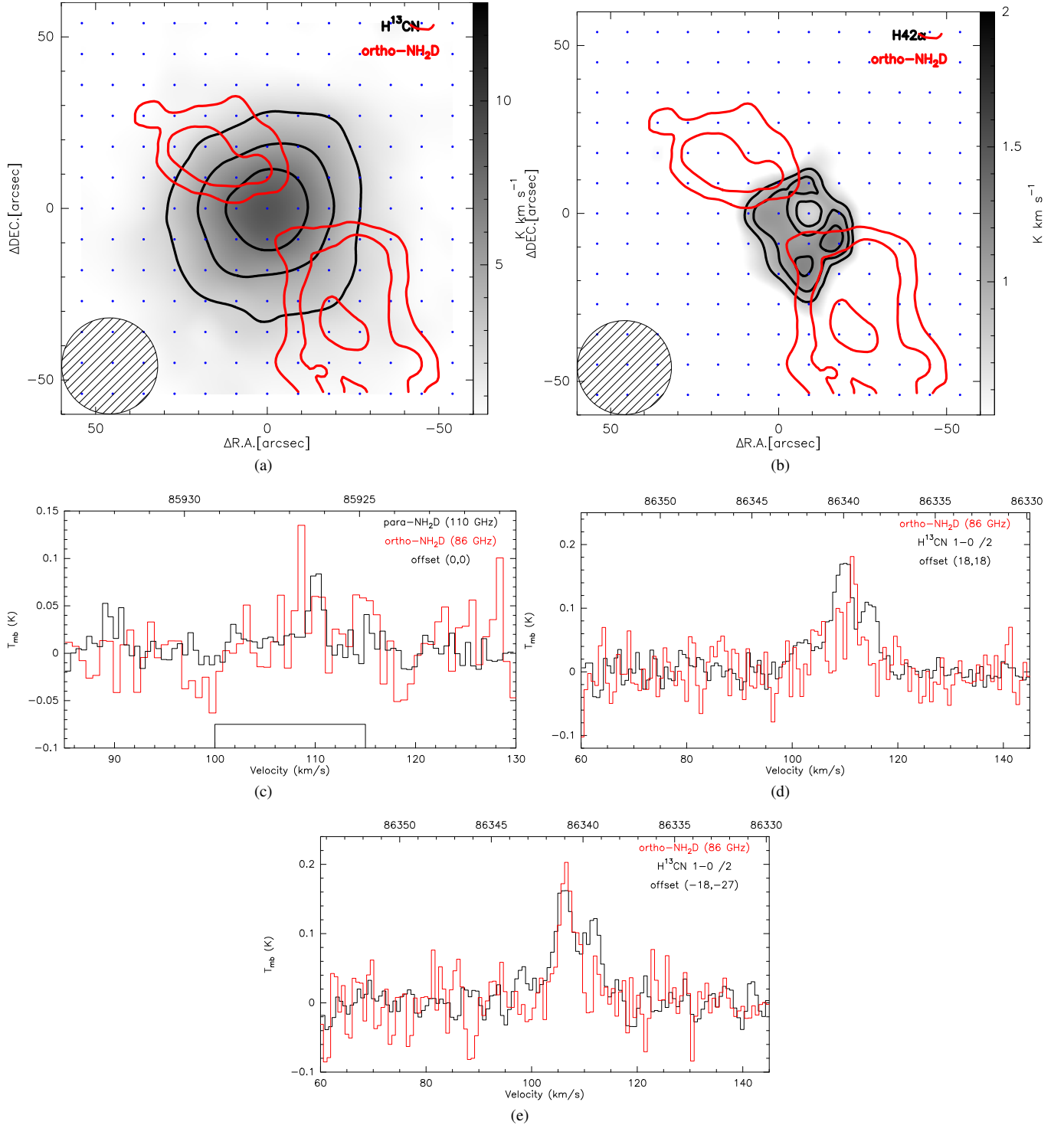


Figure 5. (a): NH_2D at 85.9263 GHz velocity integrated intensity contour (red contour) overlaid on H^{13}CN 1-0 velocity integrated intensity image (Gray scale and black contour) in G031.28+00.06. The contour levels start at 3σ in steps of 2σ for NH_2D , while the contour levels start at 18σ in steps of 15σ for H^{13}CN 1-0. The gray scale starts at 3σ . (b): NH_2D at 85.9263 GHz velocity integrated intensity contour (red contour) overlaid on $\text{H}42\alpha$ velocity integrated intensity image (Gray scale and black contour) in G031.28+00.06. The contour levels start at 3σ in steps of 3σ for NH_2D , while the contour levels start at 5σ in steps of 1σ for $\text{H}42\alpha$. The gray scale starts at 3σ . (c): Spectra of $\text{ortho-NH}_2\text{D}$ at 85.9263 GHz and $\text{para-NH}_2\text{D}$ at 110.1535 GHz in G031.28+00.06. The $\text{para-NH}_2\text{D}$ was observed by IRAM-30m with position-switching mode. The red spectra is $\text{ortho-NH}_2\text{D}$ and the black is $\text{para-NH}_2\text{D}$. The offset for two spectra is $(0'',0'')$. The black box in the picture indicates the range of flux integration of $\text{ortho-NH}_2\text{D}$ at 85.9263 GHz. (d): Spectra of $\text{ortho-NH}_2\text{D}$ at 85.9263 GHz and H^{13}CN 1-0 in G031.28+00.06. The red spectra is $\text{ortho-NH}_2\text{D}$ and the black is H^{13}CN 1-0. The offset for two spectra is $(+18'',+18'')$. (e): Spectra of $\text{ortho-NH}_2\text{D}$ at 85.9263 GHz and H^{13}CN 1-0 in G031.28+00.06. The red spectra is $\text{ortho-NH}_2\text{D}$ and the black is H^{13}CN 1-0. The offset for two spectra is $(-18'',-27'')$.

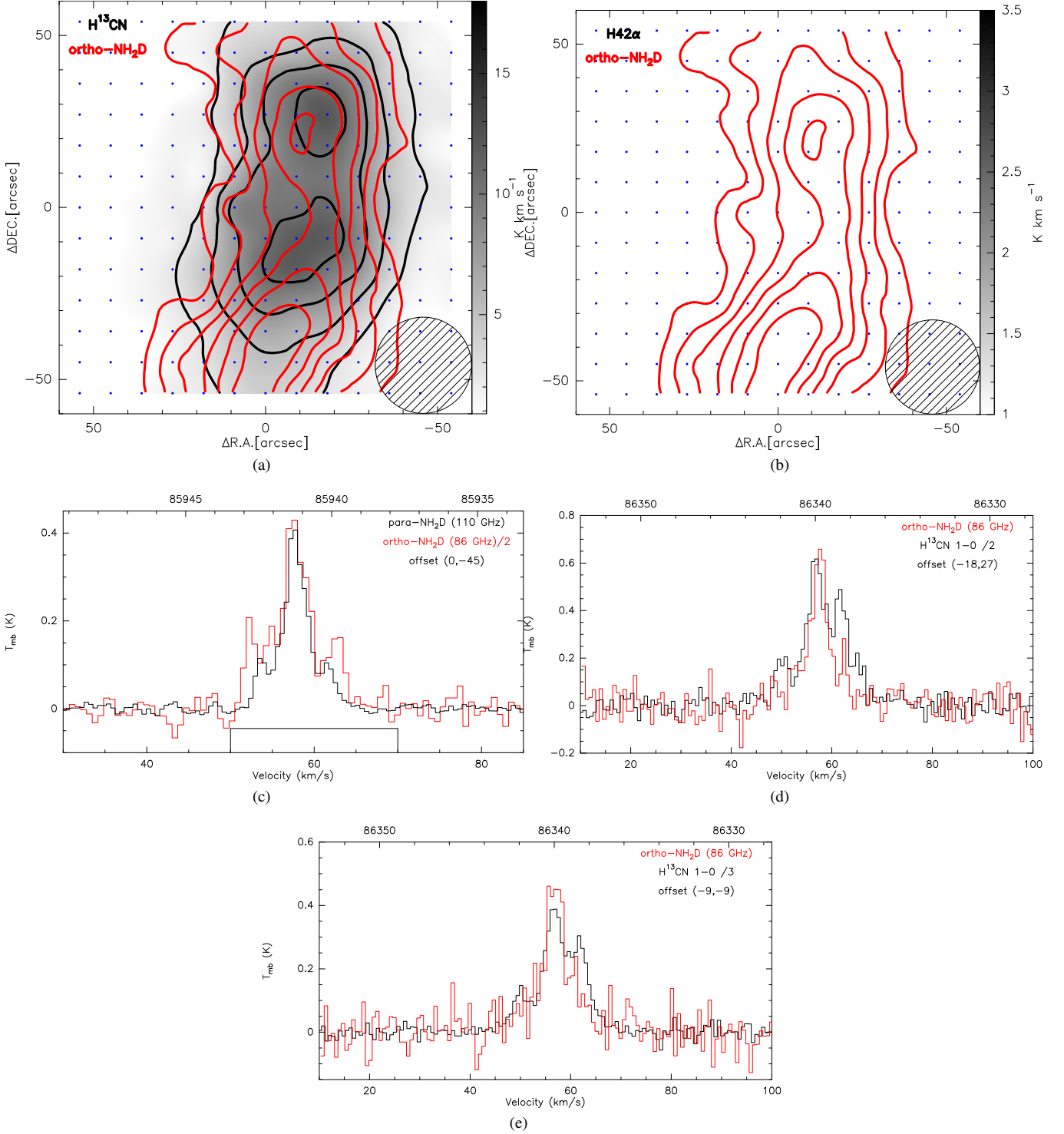


Figure 6. (a): NH₂D at 85.9263 GHz velocity integrated intensity contour (red contour) overlaid on H¹³CN 1-0 velocity integrated intensity image (Gray scale and black contour) in G034.39+00.22. The contour levels start at 5σ in steps of 3σ for NH₂D, while the contour levels start at 9σ in steps of 9σ for H¹³CN 1-0. The gray scale starts at 3σ. (b): NH₂D at 85.9263 GHz velocity integrated intensity contour (red contour) overlaid on H42α velocity integrated intensity image (Gray scale and black contour, while the H42α is not detected) in G034.39+00.22. The contour levels start at 5σ in steps of 3σ for NH₂D. (c): Spectra of ortho-NH₂D at 85.9263 GHz and para-NH₂D at 110.1535 GHz in G034.39+00.22. The para-NH₂D was observed by IRAM-30m with position-switching mode. The red spectra is ortho-NH₂D and the black is para-NH₂D. The offset for two spectra is (0′′, -45′′). The black box in the picture indicates the range of flux integration of ortho-NH₂D at 85.9263 GHz. (d): Spectra of ortho-NH₂D at 85.9263 GHz and H¹³CN 1-0 in G034.39+00.22. The red spectra is ortho-NH₂D and the black is H¹³CN 1-0. The offset for two spectra is (-18′′, -27′′). (e): Spectra of ortho-NH₂D at 85.9263 GHz and H¹³CN 1-0 in G034.39+00.22. The red spectra is ortho-NH₂D and the black is H¹³CN 1-0. The offset for two spectra is (-9′′, -9′′).

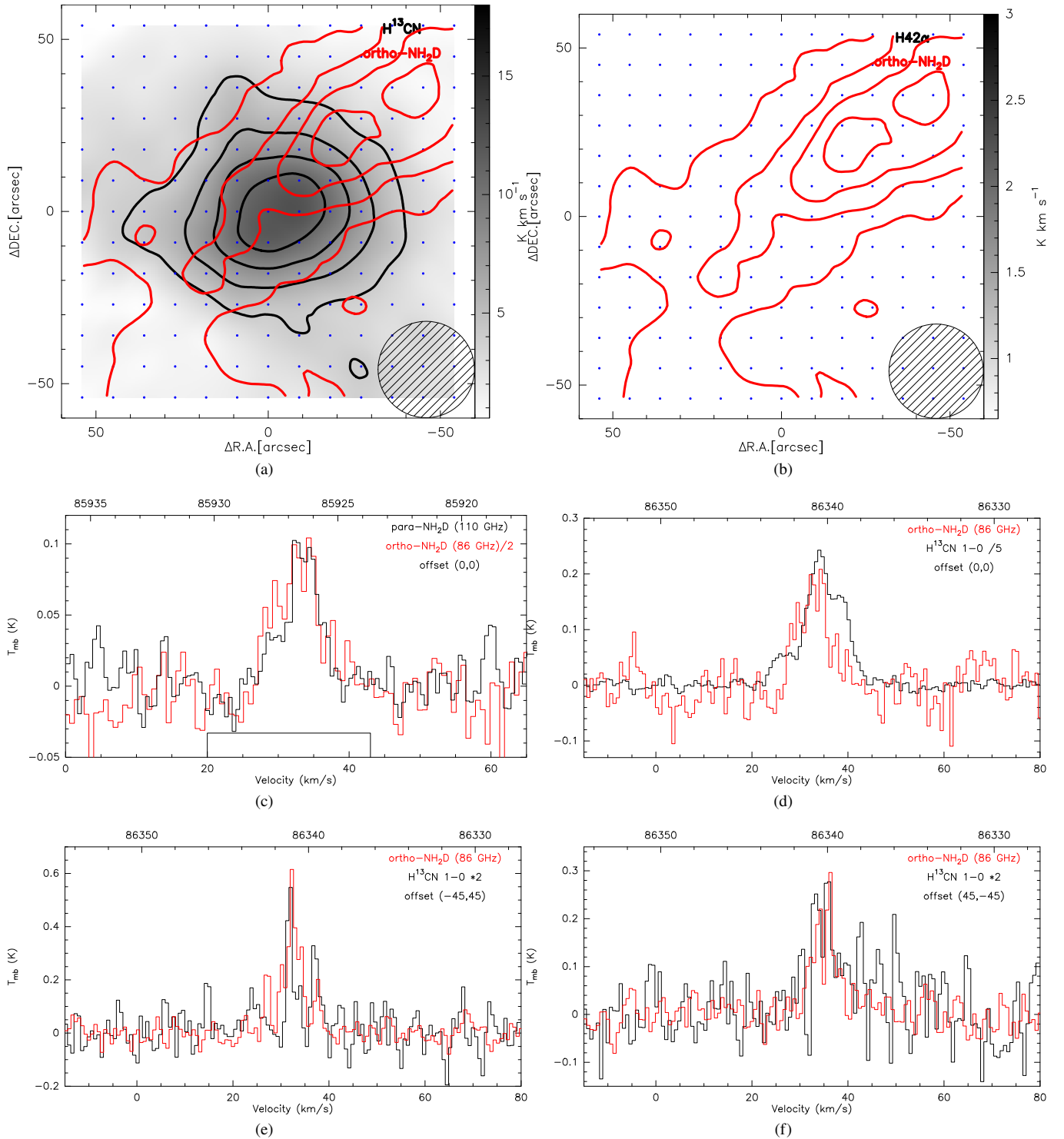


Figure 7. (a): NH_2D at 85.9263 GHz velocity integrated intensity contour (red contour) overlaid on H^{13}CN 1-0 velocity integrated intensity image (Gray scale and black contour) in G035.19-00.74. The contour levels start at 5σ in steps of 5σ for NH_2D , while the contour levels start at 21σ in steps of 12σ for H^{13}CN 1-0. The gray scale starts at 3σ . (b): NH_2D at 85.9263 GHz velocity integrated intensity contour (red contour) overlaid on $\text{H}42\alpha$ velocity integrated intensity image (Gray scale and black contour, while the $\text{H}42\alpha$ is not detected) in G035.19-00.74. The contour levels start at 5σ in steps of 5σ for NH_2D . (c): Spectra of ortho- NH_2D at 85.9263 GHz and para- NH_2D at 110.1535 GHz in G035.19-00.74. The para- NH_2D was observed by IRAM-30m with position-switching mode. The red spectra is ortho- NH_2D and the black is para- NH_2D . The offset for two spectra is $(0'', 0'')$. The black box in the picture indicates the range of flux integration of ortho- NH_2D at 85.9263 GHz. (d): Spectra of ortho- NH_2D at 85.9263 GHz and H^{13}CN 1-0 in G035.19-00.74. The red spectra is ortho- NH_2D and the black is H^{13}CN 1-0. The offset for two spectra is $(0'', 0'')$. (e): Spectra of ortho- NH_2D at 85.9263 GHz and H^{13}CN 1-0 in G035.19-00.74. The red spectra is ortho- NH_2D and the black is H^{13}CN 1-0. The offset for two spectra is $(-45'', 45'')$. (f): Spectra of ortho- NH_2D at 85.9263 GHz and H^{13}CN 1-0 in G035.19-00.74. The red spectra is ortho- NH_2D and the black is H^{13}CN 1-0. The offset for two spectra is $(45'', -45'')$.

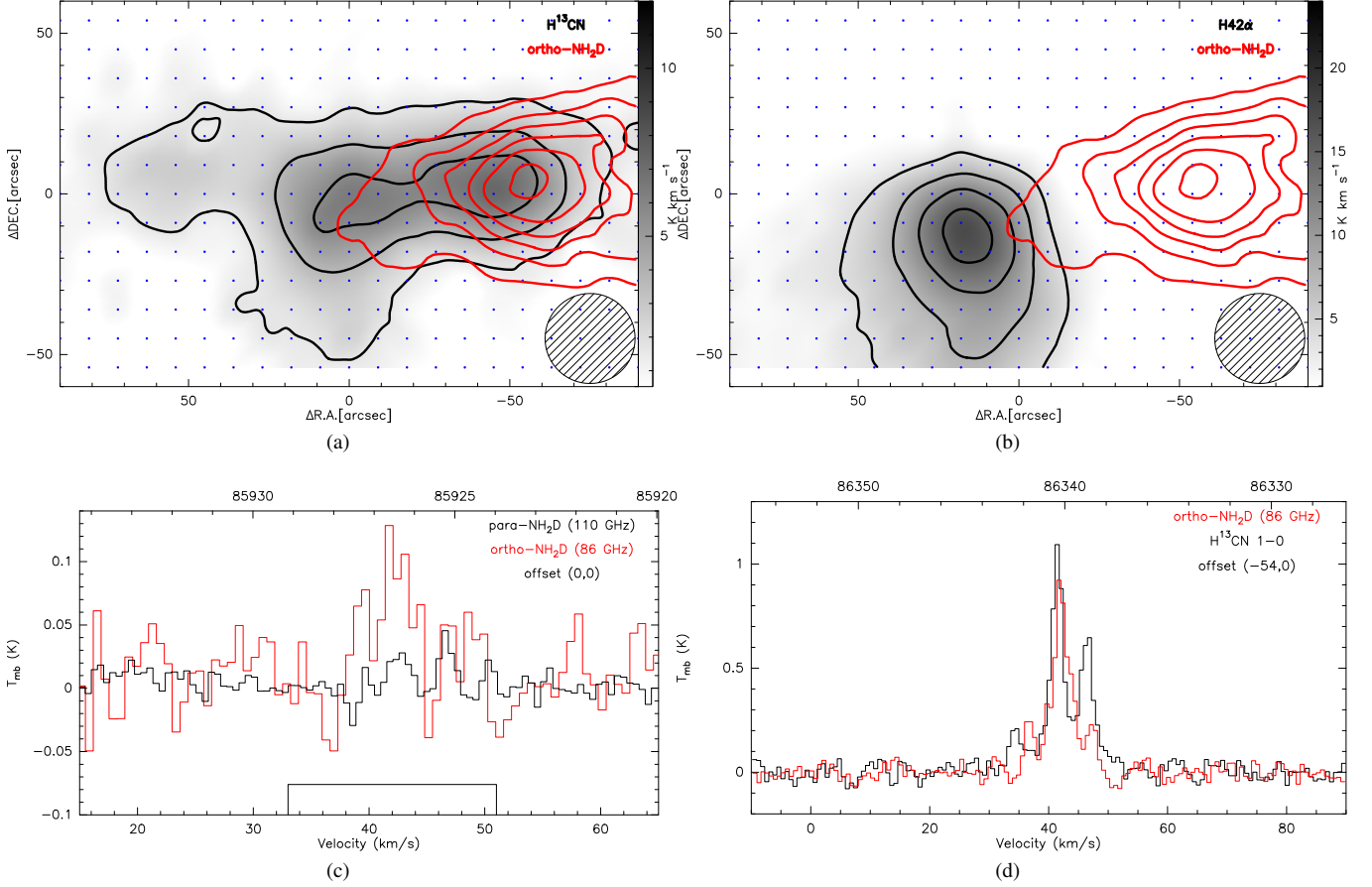


Figure 8. (a): NH_2D at 85.9263 GHz velocity integrated intensity contour (red contour) overlaid on H^{13}CN 1-0 velocity integrated intensity image (Gray scale and black contour) in G035.20-01.73. The contour levels start at 5σ in steps of 5σ for NH_2D , while the contour levels start at 9σ in steps of 12σ for H^{13}CN 1-0. The gray scale starts at 3σ . (b): NH_2D at 85.9263 GHz velocity integrated intensity contour (red contour) overlaid on $\text{H}42\alpha$ velocity integrated intensity image (Gray scale and black contour) in G035.20-01.73. The contour levels start at 5σ in steps of 5σ for NH_2D , while the contour levels start at 12σ in steps of 12σ for $\text{H}42\alpha$. The gray scale starts at 3σ . (c): Spectra of $\text{ortho-NH}_2\text{D}$ at 85.9263 GHz and $\text{para-NH}_2\text{D}$ at 110.1535 GHz in G035.20-01.73. The $\text{para-NH}_2\text{D}$ was observed by IRAM-30m with position-switching mode. The red spectra is $\text{ortho-NH}_2\text{D}$ and the black is $\text{para-NH}_2\text{D}$. The offset for two spectra is $(0'',0'')$. The black box in the picture indicates the range of flux integration of $\text{ortho-NH}_2\text{D}$ at 85.9263 GHz. (d): Spectra of $\text{ortho-NH}_2\text{D}$ at 85.9263 GHz and H^{13}CN 1-0 in G035.20-01.73. The red spectra is $\text{ortho-NH}_2\text{D}$ and the black is H^{13}CN 1-0. The offset for two spectra is $(-54'',0'')$.

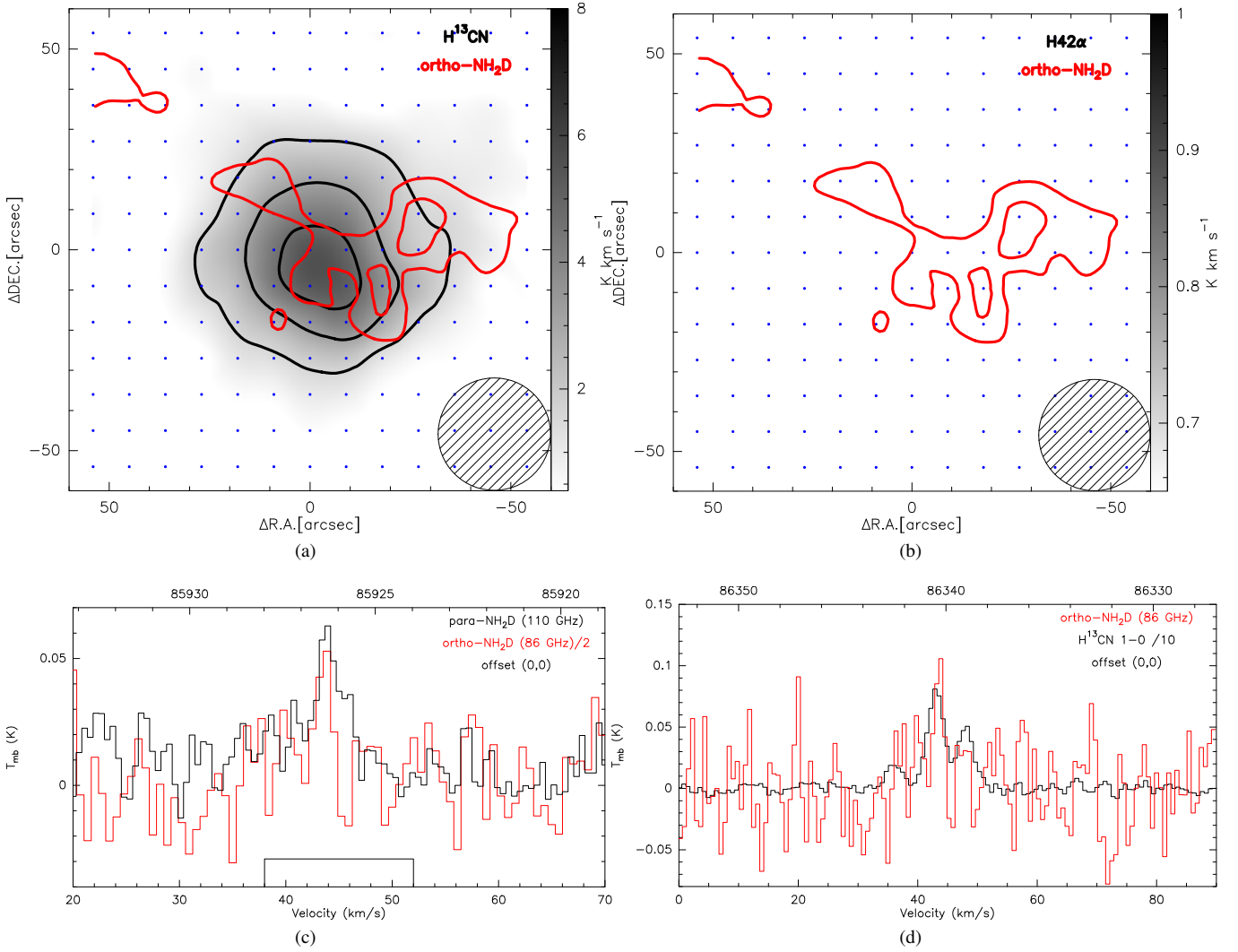


Figure 9. (a): NH_2D at 85.9263 GHz velocity integrated intensity contour (red contour) overlaid on H^{13}CN 1-0 velocity integrated intensity image (Gray scale and black contour) in G037.43+01.51. The contour levels start at 3σ in steps of 2σ for NH_2D , while the contour levels start at 12σ in steps of 12σ for H^{13}CN 1-0. The gray scale starts at 3σ . (b): NH_2D at 85.9263 GHz velocity integrated intensity contour (red contour) overlaid on $\text{H}42\alpha$ velocity integrated intensity image (Gray scale and black contour, while the $\text{H}42\alpha$ is not detected) in G037.43+01.51. The contour levels start at 3σ in steps of 2σ for NH_2D . (c): Spectra of $\text{ortho-NH}_2\text{D}$ at 85.9263 GHz and $\text{para-NH}_2\text{D}$ at 110.1535 GHz in G037.43+01.51. The $\text{para-NH}_2\text{D}$ was observed by IRAM-30m with position-switching mode. The red spectra is $\text{ortho-NH}_2\text{D}$ and the black is $\text{para-NH}_2\text{D}$. The offset for two spectra is $(0'',0'')$. The black box in the picture indicates the range of flux integration of $\text{ortho-NH}_2\text{D}$ at 85.9263 GHz. (d): Spectra of $\text{ortho-NH}_2\text{D}$ at 85.9263 GHz and H^{13}CN 1-0 in G037.43+01.51. The red spectra is $\text{ortho-NH}_2\text{D}$ and the black is H^{13}CN 1-0. The offset for two spectra is $(0'',0'')$.

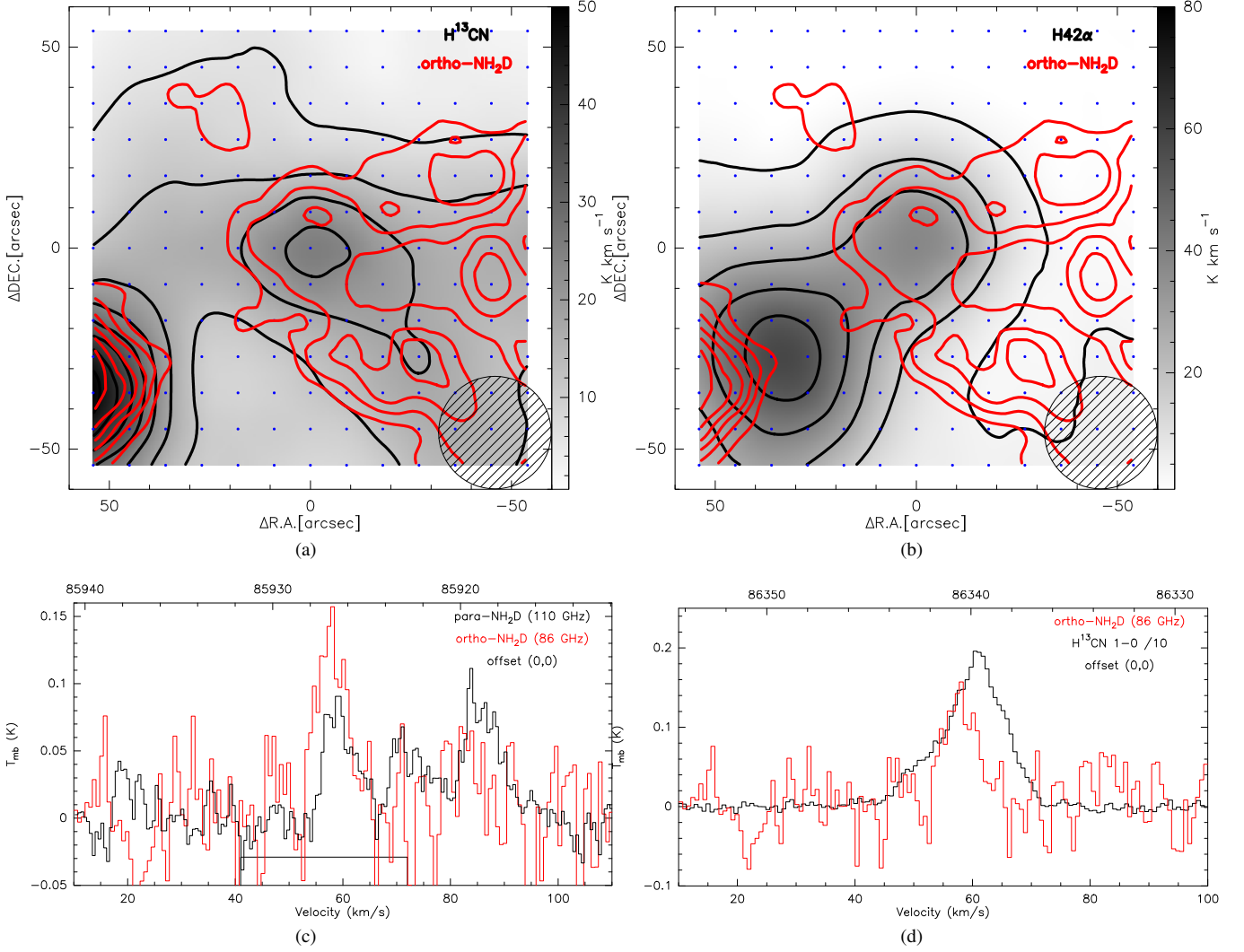


Figure 10. (a): NH₂D at 85.9263 GHz velocity integrated intensity contour (red contour) overlaid on H¹³CN 1-0 velocity integrated intensity image (Gray scale and black contour) in G049.48-00.36. The contour levels start at 5σ in steps of 2σ for NH₂D, while the contour levels start at 30σ in steps of 30σ for H¹³CN 1-0. The gray scale starts at 3σ. (b): NH₂D at 85.9263 GHz velocity integrated intensity contour (red contour) overlaid on H42α velocity integrated intensity image (Gray scale and black contour) in G049.48-00.36. The contour levels start at 5σ in steps of 2σ for NH₂D, while the contour levels start at 15σ in steps of 40σ for H42α. The gray scale starts at 3σ. (c): Spectra of ortho-NH₂D at 85.9263 GHz and para-NH₂D at 110.1535 GHz in G049.48-00.36. The para-NH₂D was observed by IRAM-30m with position-switching mode. The red spectra is ortho-NH₂D and the black is para-NH₂D. The offset for two spectra is (0′′,0′′). The black box in the picture indicates the range of flux integration of ortho-NH₂D at 85.9263 GHz. (d): Spectra of ortho-NH₂D at 85.9263 GHz and H¹³CN 1-0 in G049.48-00.36. The red spectra is ortho-NH₂D and the black is H¹³CN 1-0. The offset for two spectra is (0′′,0′′).

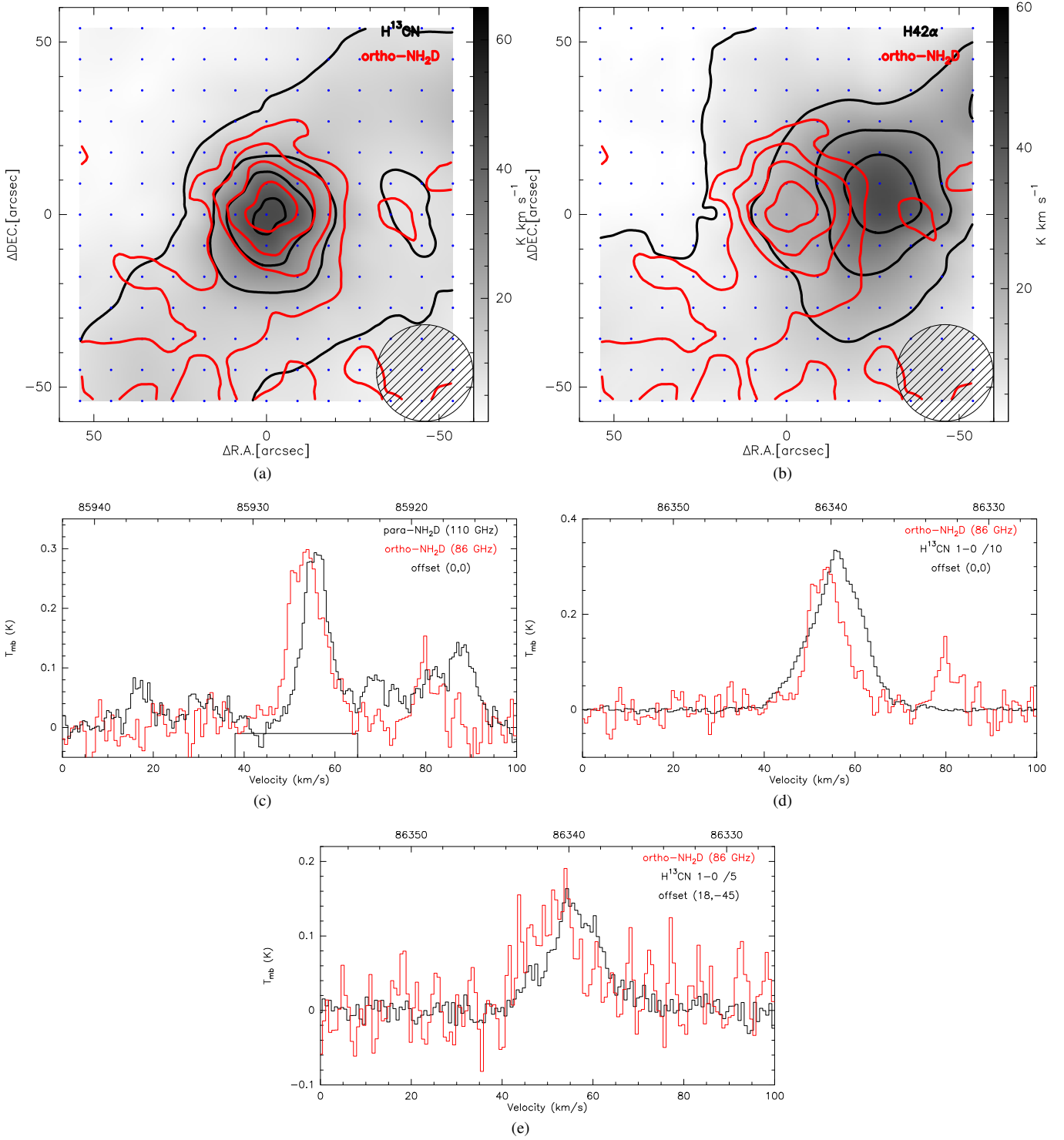


Figure 11. (a): NH₂D at 85.9263 GHz velocity integrated intensity contour (red contour) overlaid on H¹³CN 1-0 velocity integrated intensity image (Gray scale and black contour) in G049.48-00.38. The contour levels start at 4σ in steps of 3σ for NH₂D, while the contour levels start at 27σ in steps of 40σ for H¹³CN 1-0. The gray scale starts at 3σ . (b): NH₂D at 85.9263 GHz velocity integrated intensity contour (red contour) overlaid on H42 α velocity integrated intensity image (Gray scale and black contour) in G049.48-00.38. The contour levels start at 4σ in steps of 3σ for NH₂D, while the contour levels start at 9σ in steps of 30σ for H42 α . The gray scale starts at 3σ . (c): Spectra of ortho-NH₂D at 85.9263 GHz and para-NH₂D at 110.1535 GHz in G049.48-00.38. The para-NH₂D was observed by IRAM-30m with position-switching mode. The red spectra is ortho-NH₂D and the black is para-NH₂D. The offset for two spectra is (0'',0''). (d): Spectra of ortho-NH₂D at 85.9263 GHz and H¹³CN 1-0 in G049.48-00.38. The red spectra is ortho-NH₂D and the black is H¹³CN 1-0. The offset for two spectra is (0'',0''). The black box in the picture indicates the range of flux integration of ortho-NH₂D at 85.9263 GHz. (e): Spectra of ortho-NH₂D at 85.9263 GHz and H¹³CN 1-0 in G049.48-00.38. The red spectra is ortho-NH₂D and the black is H¹³CN 1-0. The offset for two spectra is (+18'', -45'').

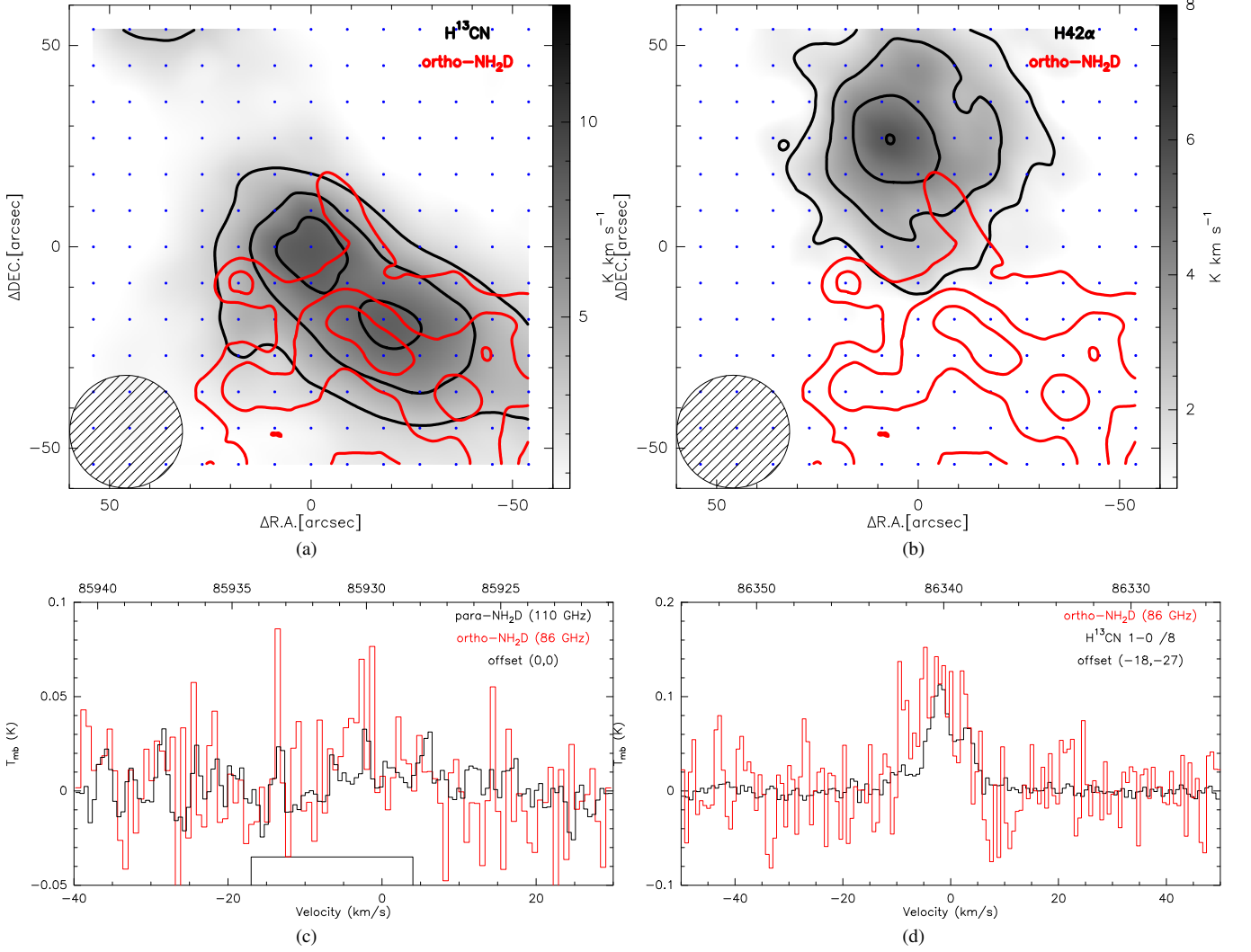


Figure 12. (a): NH₂D at 85.9263 GHz velocity integrated intensity contour (red contour) overlaid on H¹³CN 1-0 velocity integrated intensity image (Gray scale and black contour) in G075.76+00.33. The contour levels start at 3σ in steps of 2σ for NH₂D, while the contour levels start at 15σ in steps of 12σ for H¹³CN 1-0. The gray scale starts at 3σ . (b): NH₂D at 85.9263 GHz velocity integrated intensity contour (red contour) overlaid on H42α velocity integrated intensity image (Gray scale and black contour) in G075.76+00.33. The contour levels start at 3σ in steps of 2σ for NH₂D, while the contour levels start at 5σ in steps of 5σ for H42α. The gray scale starts at 3σ . (c): Spectra of ortho-NH₂D at 85.9263 GHz and para-NH₂D at 110.1535 GHz in G075.76+00.33. The para-NH₂D was observed by IRAM-30m with position-switching mode. The red spectra is ortho-NH₂D and the black is para-NH₂D. The offset for two spectra is (0'', 0''). The black box in the picture indicates the range of flux integration of ortho-NH₂D at 85.9263 GHz. (d): Spectra of ortho-NH₂D at 85.9263 GHz and H¹³CN 1-0 in G075.76+00.33. The red spectra is ortho-NH₂D and the black is H¹³CN 1-0. The offset for two spectra is (-18'', -27'').

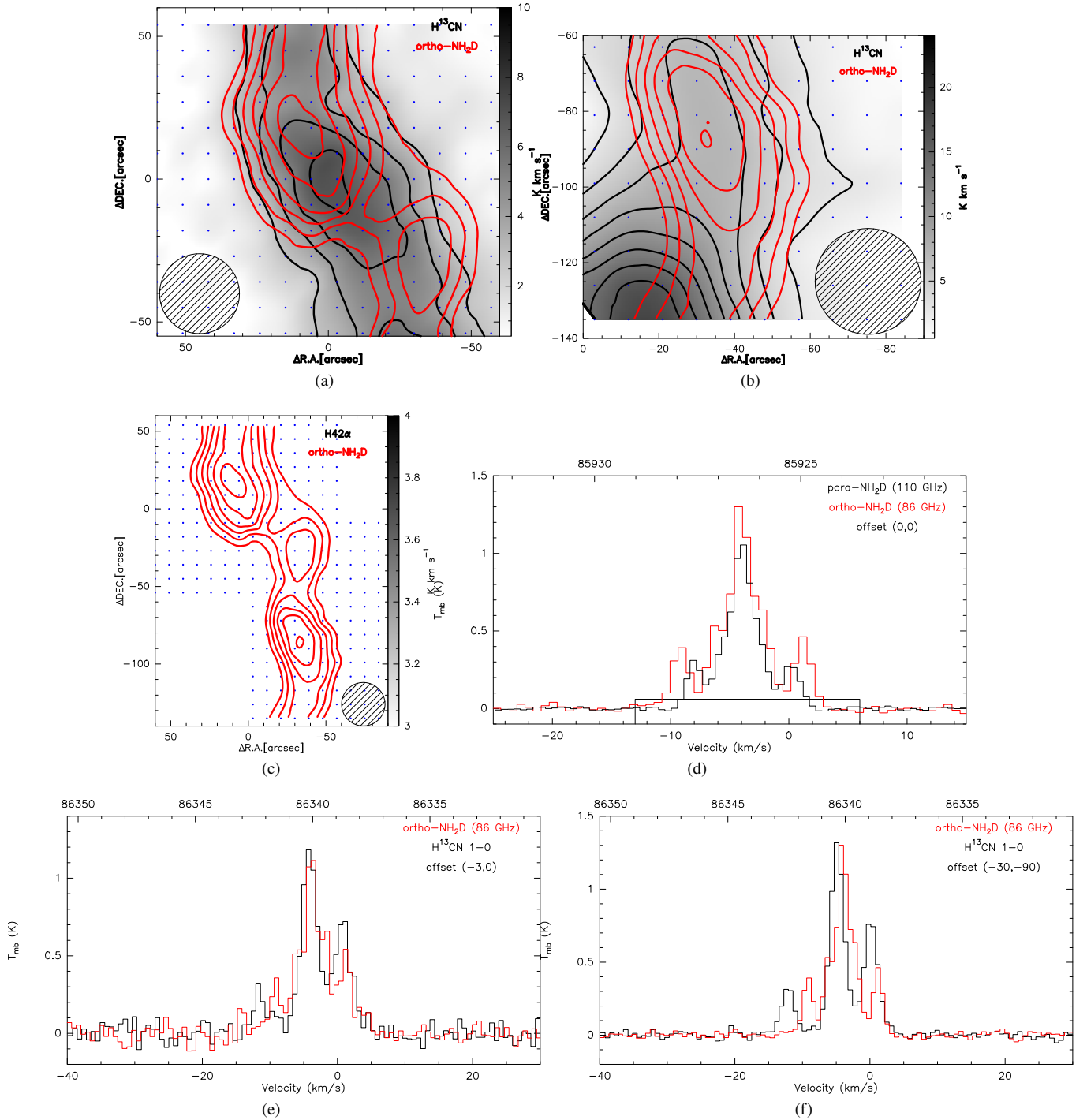


Figure 13. (a): NH_2D at 85.9263 GHz velocity integrated intensity contour (red contour) overlaid on H^{13}CN 1-0 velocity integrated intensity image (Gray scale and black contour) in G081.75+00.59 (W 75S). The contour levels start at 18σ in steps of 5σ for NH_2D , while the contour levels start at 15σ in steps of 7σ for H^{13}CN 1-0. The gray scale starts at 3σ . (b): NH_2D at 85.9263 GHz velocity integrated intensity contour (red contour) overlaid on H^{13}CN 1-0 velocity integrated intensity image (Gray scale and black contour) in G081.75+00.59 (DR 21(OH)). The contour levels start at 18σ in steps of 5σ for NH_2D , while the contour levels start at 15σ in steps of 10σ for H^{13}CN 1-0. The gray scale starts at 3σ . (c): NH_2D at 85.9263 GHz velocity integrated intensity contour (red contour) overlaid on $\text{H}42\alpha$ velocity integrated intensity image (Gray scale and black contour, while the $\text{H}42\alpha$ is not detected) in G081.75+00.59. The contour levels start at 18σ in steps of 5σ for NH_2D . (d): Spectra of $\text{ortho-NH}_2\text{D}$ at 85.9263 GHz and $\text{para-NH}_2\text{D}$ at 110.1535 GHz in G081.75+00.59. The $\text{para-NH}_2\text{D}$ was observed by IRAM-30m with position-switching mode. The red spectra is $\text{ortho-NH}_2\text{D}$ and the black is $\text{para-NH}_2\text{D}$. The offset for two spectra is $(0'', -3'')$. The black box in the picture indicates the range of flux integration of $\text{ortho-NH}_2\text{D}$ at 85.9263 GHz. (e): Spectra of $\text{ortho-NH}_2\text{D}$ at 85.9263 GHz and H^{13}CN 1-0 in G081.75+00.59. The red spectra is $\text{ortho-NH}_2\text{D}$ and the black is H^{13}CN 1-0. The offset for two spectra is $(-3'', 0'')$. (f): Spectra of $\text{ortho-NH}_2\text{D}$ at 85.9263 GHz and H^{13}CN 1-0 in G081.75+00.59. The red spectra is $\text{ortho-NH}_2\text{D}$ and the black is H^{13}CN 1-0. The offset for two spectra is $(-30'', -90'')$.

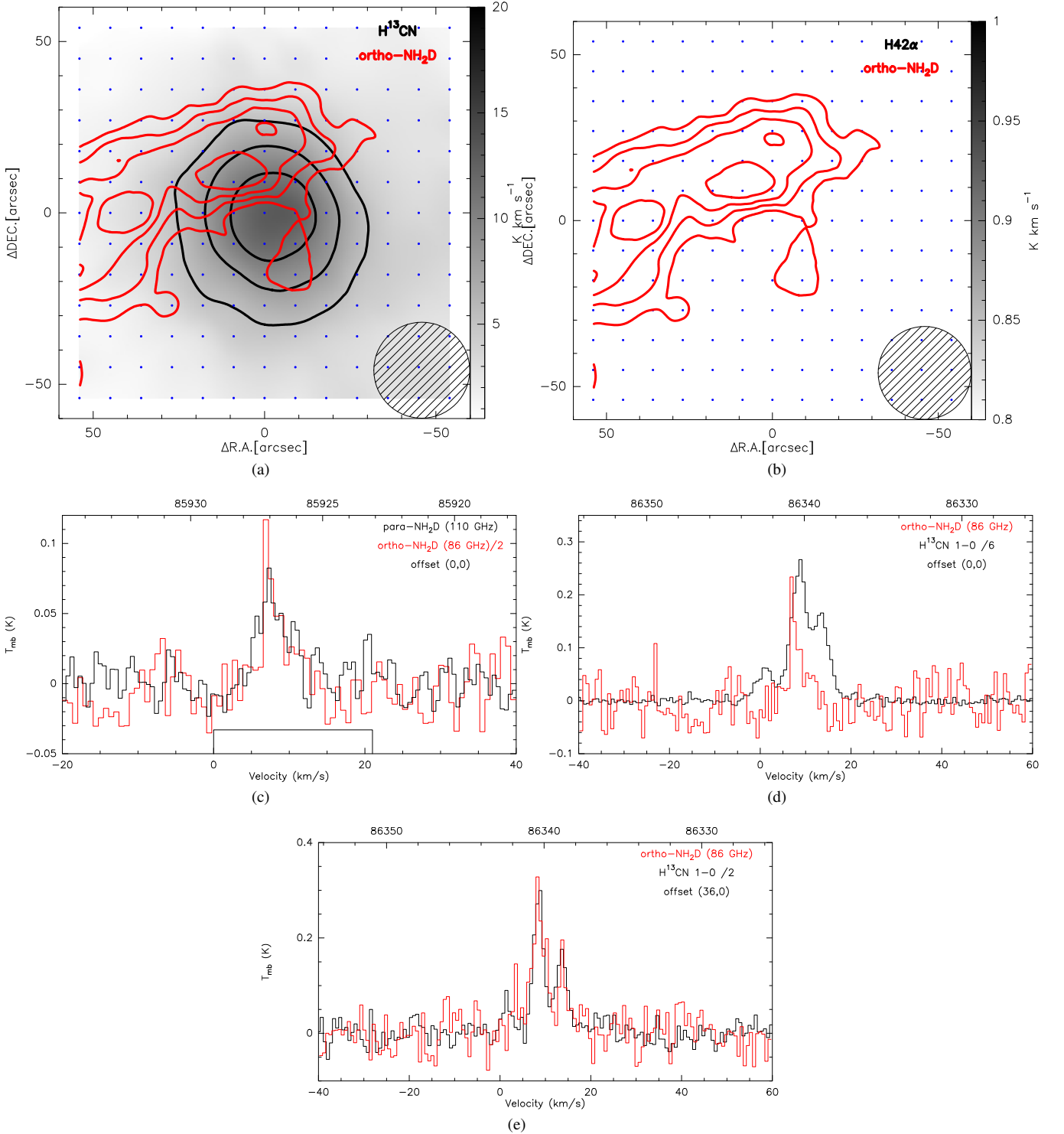


Figure 14. (a): NH₂D at 85.9263 GHz velocity integrated intensity contour (red contour) overlaid on H¹³CN 1-0 velocity integrated intensity image (Gray scale and black contour) in G081.87+00.78. The contour levels start at 5σ in steps of 2σ for NH₂D, while the contour levels start at 30σ in steps of 15σ for H¹³CN 1-0. The gray scale starts at 3σ. (b): NH₂D at 85.9263 GHz velocity integrated intensity contour (red contour) overlaid on H42α velocity integrated intensity image (Gray scale and black contour, while the H42α is not detected) in G081.87+00.78. The contour levels start at 5σ in steps of 2σ for NH₂D. (c): Spectra of ortho-NH₂D at 85.9263 GHz and para-NH₂D at 110.1535 GHz in G081.87+00.78. The para-NH₂D was observed by IRAM-30m with position-switching mode. The red spectra is ortho-NH₂D and the black is para-NH₂D. The offset for two spectra is (0′′,0′′). The black box in the picture indicates the range of flux integration of ortho-NH₂D at 85.9263 GHz. (d): Spectra of ortho-NH₂D at 85.9263 GHz and H¹³CN 1-0 in G081.87+00.78. The red spectra is ortho-NH₂D and the black is H¹³CN 1-0. The offset for two spectra is (0′′,0′′). (e): Spectra of ortho-NH₂D at 85.9263 GHz and H¹³CN 1-0 in G081.87+00.78. The red spectra is ortho-NH₂D and the black is H¹³CN 1-0. The offset for two spectra is (+36′′,0′′).

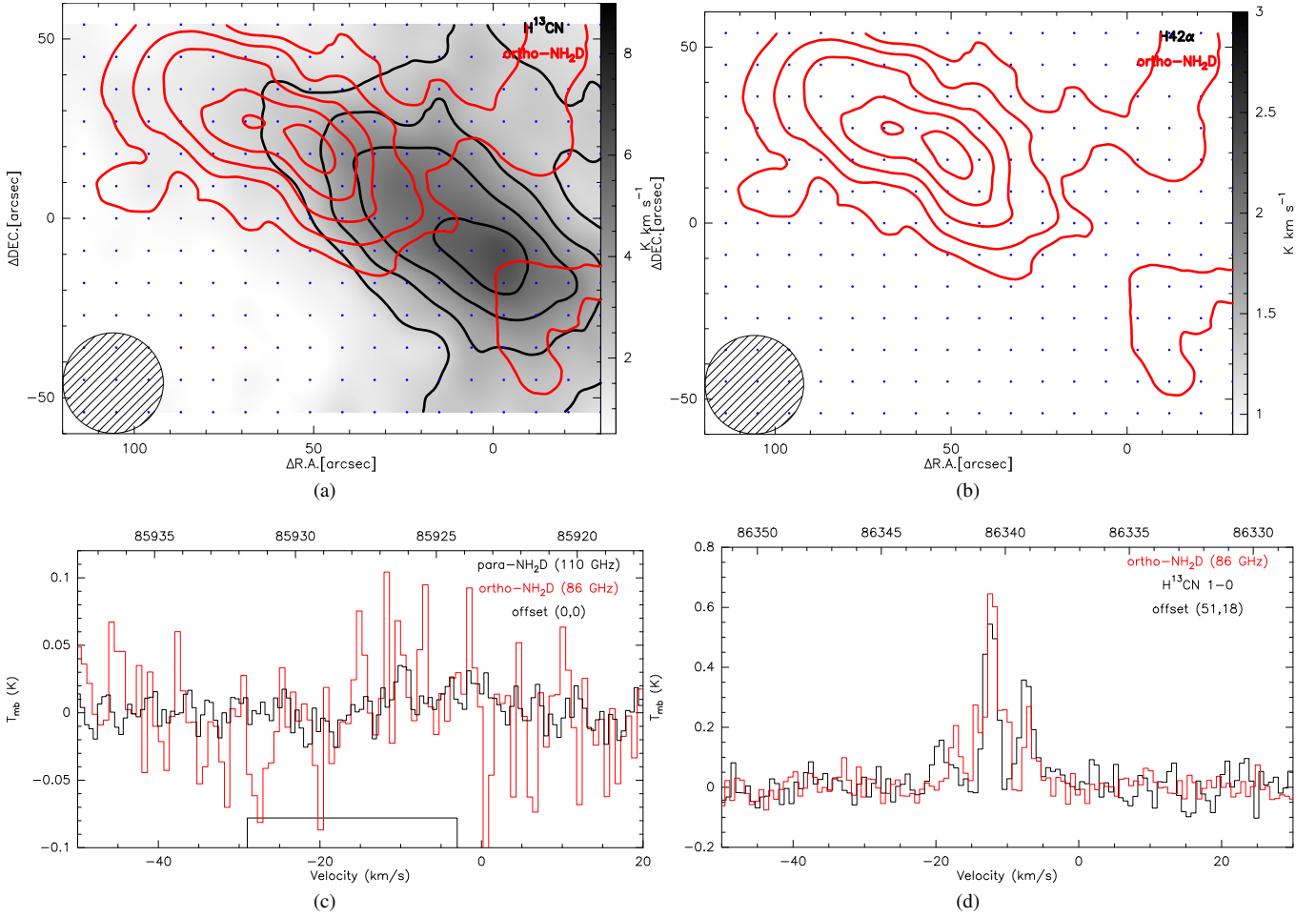


Figure 15. (a): NH_2D at 85.9263 GHz velocity integrated intensity contour (red contour) overlaid on H^{13}CN 1-0 velocity integrated intensity image (Gray scale and black contour) in G109.87+02.11. The contour levels start at 3σ in steps of 3σ for NH_2D , while the contour levels start at 12σ in steps of 7σ for H^{13}CN 1-0. The gray scale starts at 3σ . (b): NH_2D at 85.9263 GHz velocity integrated intensity contour (red contour) overlaid on $\text{H}42\alpha$ velocity integrated intensity image (Gray scale and black contour, while the $\text{H}42\alpha$ is not detected) in G109.87+02.11. The contour levels start at 3σ in steps of 3σ for NH_2D . (c): Spectra of $\text{ortho-NH}_2\text{D}$ at 85.9263 GHz and $\text{para-NH}_2\text{D}$ at 110.1535 GHz in G109.87+02.11. The $\text{para-NH}_2\text{D}$ was observed by IRAM-30m with position-switching mode. The red spectra is $\text{ortho-NH}_2\text{D}$ and the black is $\text{para-NH}_2\text{D}$. The offset for two spectra is (0'', 0''). The black box in the picture indicates the range of flux integration of $\text{ortho-NH}_2\text{D}$ at 85.9263 GHz. (d): Spectra of $\text{ortho-NH}_2\text{D}$ at 85.9263 GHz and H^{13}CN 1-0 in G109.87+02.11. The red spectra is $\text{ortho-NH}_2\text{D}$ and the black is H^{13}CN 1-0. The offset for two spectra is (+51'', +18'').

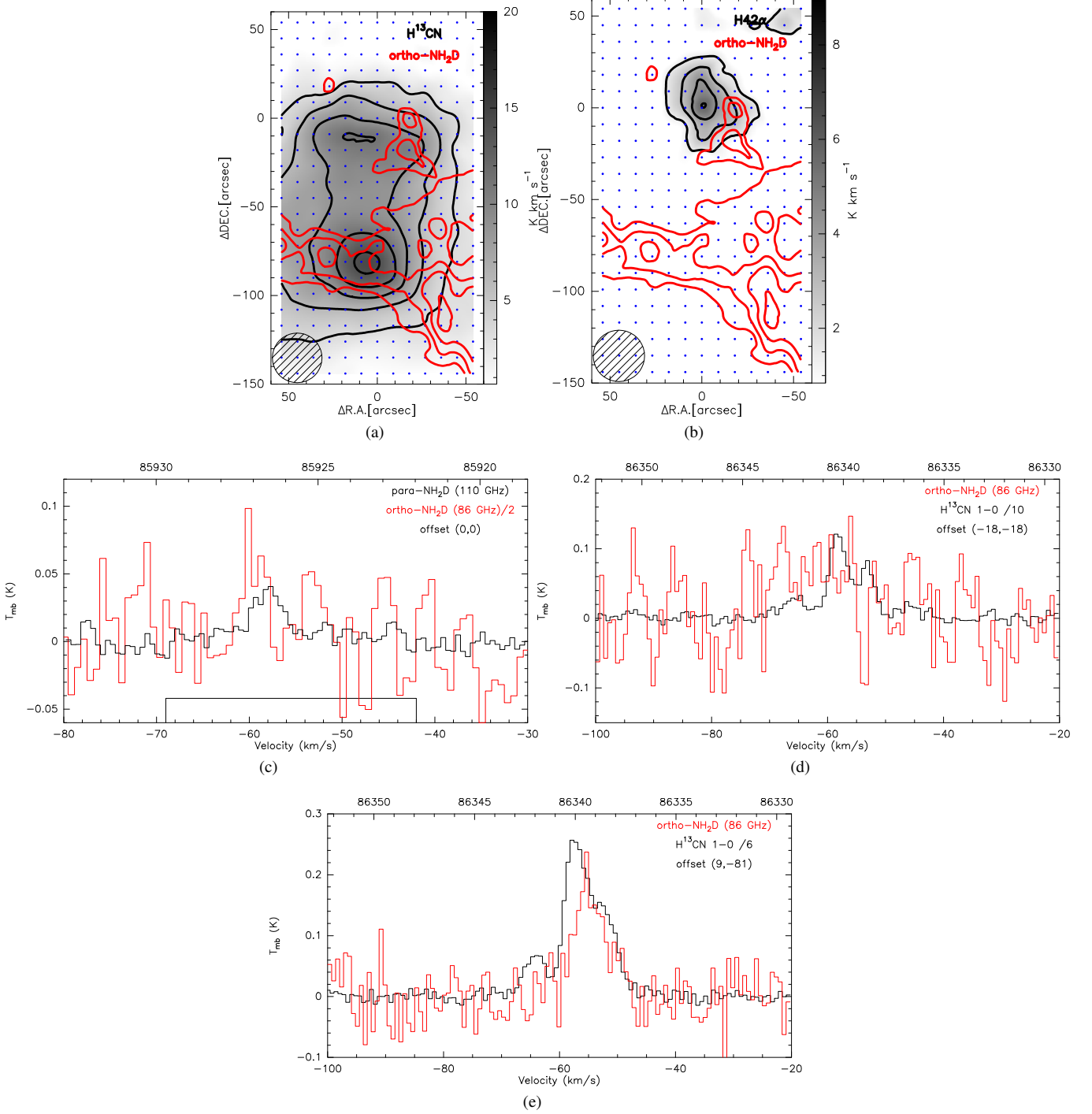


Figure 16. (a): NH₂D at 85.9263 GHz velocity integrated intensity contour (red contour) overlaid on H¹³CN 1-0 velocity integrated intensity image (Gray scale and black contour) in G111.54+00.77. The contour levels start at 3σ in steps of 2σ for NH₂D, while the contour levels start at 15σ in steps of 12σ for H¹³CN 1-0. The gray scale starts at 3σ . (b): NH₂D at 85.9263 GHz velocity integrated intensity contour (red contour) overlaid on H42 α velocity integrated intensity image (Gray scale and black contour) in G111.54+00.77. The contour levels start at 3σ in steps of 2σ for NH₂D, while the contour levels start at 5σ in steps of 5σ for H42 α . The gray scale starts at 3σ . (c): Spectra of ortho-NH₂D at 85.9263 GHz and para-NH₂D at 110.1535 GHz in G111.54+00.77. The para-NH₂D was observed by IRAM-30m with position-switching mode. The red spectra is ortho-NH₂D and the black is para-NH₂D. The offset for two spectra is (0'',0''). The black box in the picture indicates the range of flux integration of ortho-NH₂D at 85.9263 GHz. (d): Spectra of ortho-NH₂D at 85.9263 GHz and H¹³CN 1-0 in G111.54+00.77. The red spectra is ortho-NH₂D and the black is H¹³CN 1-0. The offset for two spectra is (-18'',-18''). (e): Spectra of ortho-NH₂D at 85.9263 GHz and H¹³CN 1-0 in G049.48-00.38. The red spectra is ortho-NH₂D and the black is H¹³CN 1-0. The offset for two spectra is (+9'',-81'').

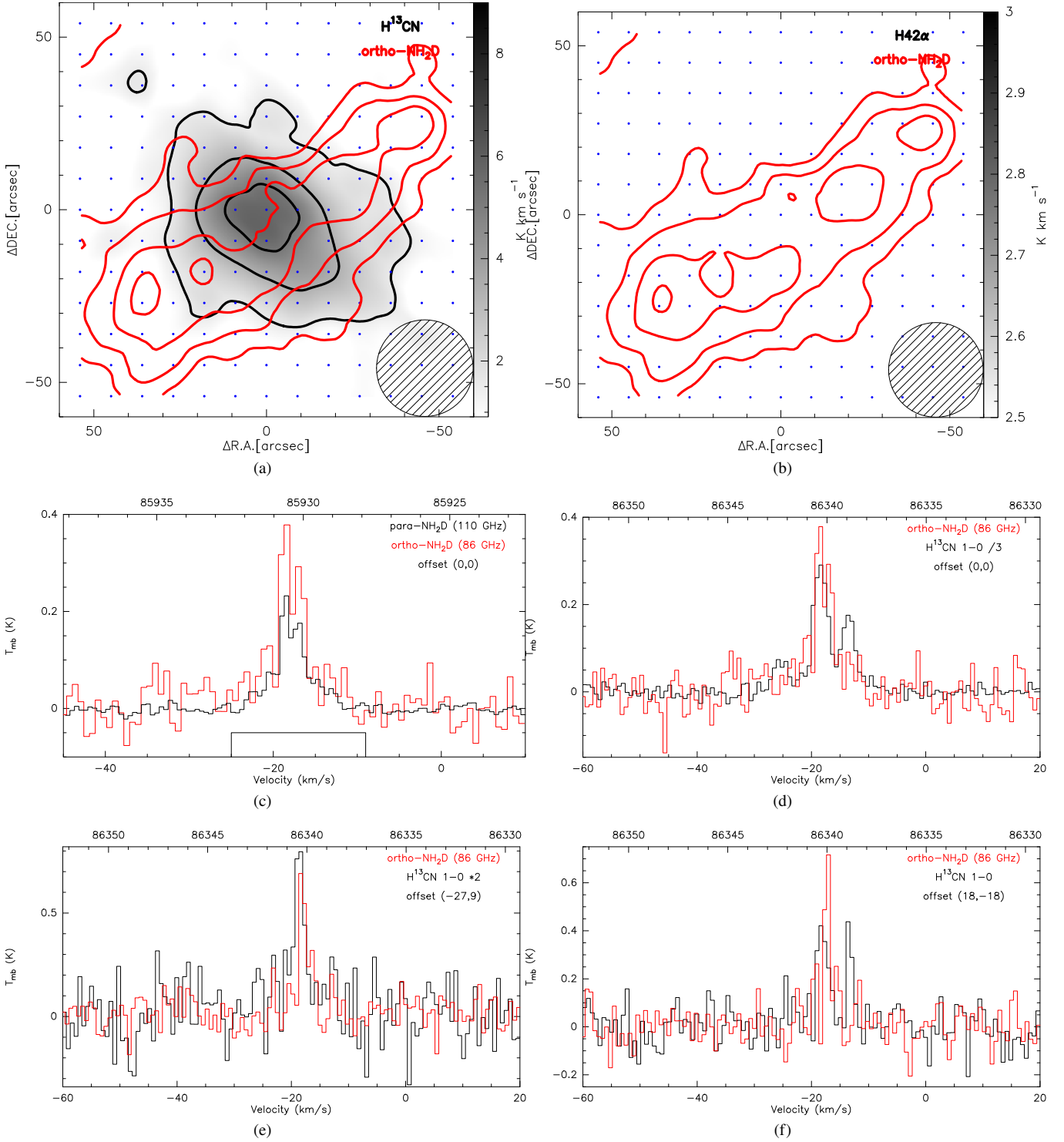


Figure 17. (a): NH₂D at 85.9263 GHz velocity integrated intensity contour (red contour) overlaid on H¹³CN 1-0 velocity integrated intensity image (Gray scale and black contour) in G121.29+00.65. The contour levels start at 3σ in steps of 2σ for NH₂D, while the contour levels start at 5σ in steps of 6σ for H¹³CN 1-0. The gray scale starts at 3σ . (b): NH₂D at 85.9263 GHz velocity integrated intensity contour (red contour) overlaid on H42α velocity integrated intensity image (Gray scale and black contour, while the H42α is not detected) in G121.29+00.65. The contour levels start at 3σ in steps of 1σ for NH₂D. (c): Spectra of ortho-NH₂D at 85.9263 GHz and para-NH₂D at 110.1535 GHz in G121.29+00.65. The para-NH₂D was observed by IRAM-30m with position-switching mode. The red spectra is ortho-NH₂D and the black is para-NH₂D. The offset for two spectra is (0'',0''). The black box in the picture indicates the range of flux integration of ortho-NH₂D at 85.9263 GHz. (d): Spectra of ortho-NH₂D at 85.9263 GHz and H¹³CN 1-0 in G121.29+00.65. The red spectra is ortho-NH₂D and the black is H¹³CN 1-0. The offset for two spectra is (0'',0''). (e): Spectra of ortho-NH₂D at 85.9263 GHz and H¹³CN 1-0 in G121.29+00.65. The red spectra is ortho-NH₂D and the black is H¹³CN 1-0. The offset for two spectra is (-27'',9''). (f): Spectra of ortho-NH₂D at 85.9263 GHz and H¹³CN 1-0 in G121.29+00.65. The red spectra is ortho-NH₂D and the black is H¹³CN 1-0. The offset for two spectra is (18'',-18'').

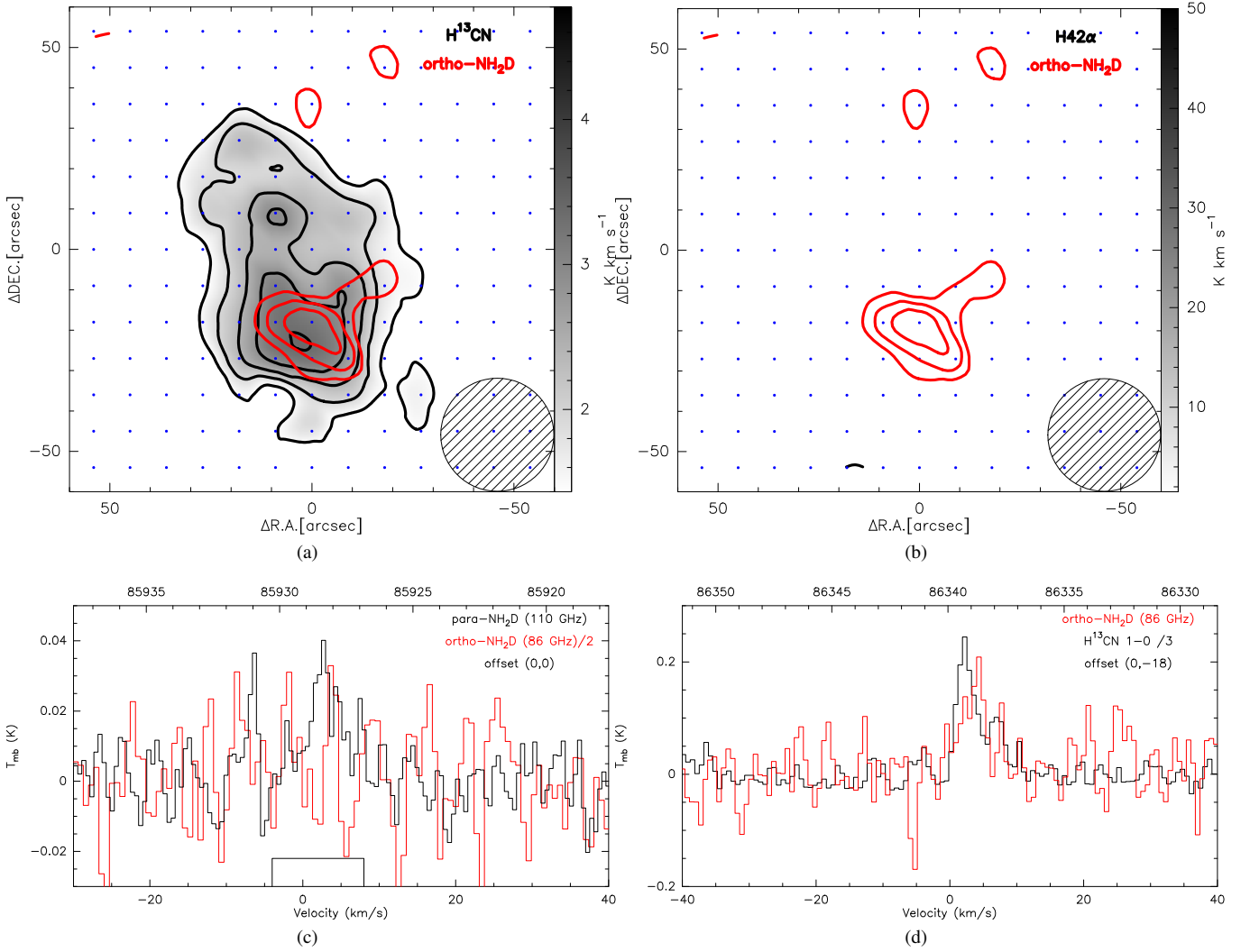


Figure 18. (a): NH_2D at 85.9263 GHz velocity integrated intensity contour (red contour) overlaid on H^{13}CN 1-0 velocity integrated intensity image (Gray scale and black contour) in G188.94+00.88. The contour levels start at 3σ in steps of 1σ for NH_2D , while the contour levels start at 5σ in steps of 2σ for H^{13}CN 1-0. The gray scale starts at 3σ . (b): NH_2D at 85.9263 GHz velocity integrated intensity contour (red contour) overlaid on $\text{H}42\alpha$ velocity integrated intensity image (Gray scale and black contour, while the $\text{H}42\alpha$ is not detected) in G188.94+00.88. The contour levels start at 3σ in steps of 1σ for NH_2D . (c): Spectra of ortho- NH_2D at 85.9263 GHz and para- NH_2D at 110.1535 GHz in G188.94+00.88. The para- NH_2D was observed by IRAM-30m with position-switching mode. The red spectra is ortho- NH_2D and the black is para- NH_2D . The offset for two spectra is $(0'', 0'')$. The black box in the picture indicates the range of flux integration of ortho- NH_2D at 85.9263 GHz. (d): Spectra of ortho- NH_2D at 85.9263 GHz and H^{13}CN 1-0 in G188.94+00.88. The red spectra is ortho- NH_2D and the black is H^{13}CN 1-0. The offset for two spectra is $(0'', -18'')$.

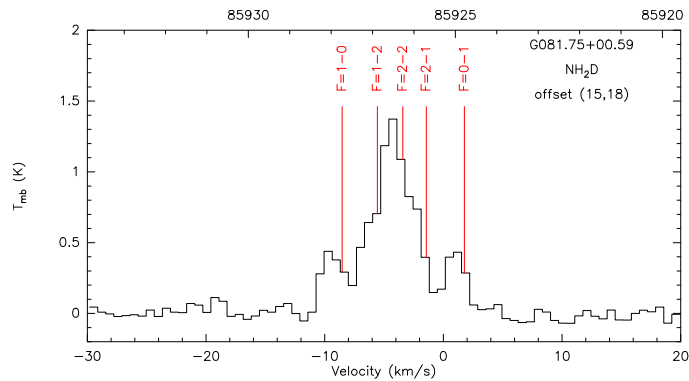


Figure 19. The hyperfine structure of ortho- NH_2D in G081.75+00.59.

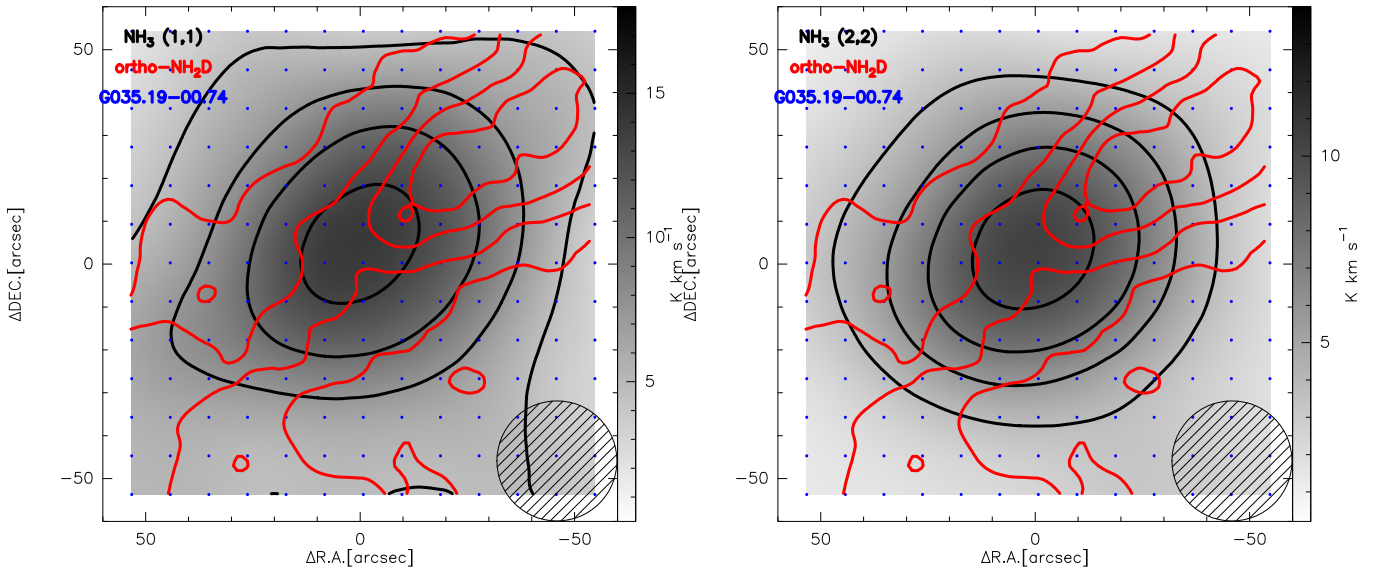


Figure 20. (a): NH_2D at 85.926 GHz velocity integrated intensity contour (red contour) overlaid on $NH_3(1,1)$ main group velocity integrated intensity image (Gray scale and black contour) in G035.19-00.74. The contour levels start at 5σ in steps of 5σ for NH_2D , while the contour levels start at 90σ in steps of 54σ for $NH_3(1,1)$ main group. The gray scale starts at 3σ . (b): NH_2D at 85.926 GHz velocity integrated intensity contour (red contour) overlaid on $NH_3(2,2)$ main group velocity integrated intensity image (Gray scale and black contour) in G035.19-00.74. The contour levels start at 5σ in steps of 5σ for NH_2D , while the contour levels start at 54σ in steps of 27σ for $NH_3(2,2)$ main group. The gray scale starts at 3σ .